

INVESTIGATION OF SOLIDIFICATION OF
HIGH-STRENGTH STEEL CASTINGS

AMMRC CR 63-04/5

INTERIM REPORT

by

M. C. Flemings, R. V. Barone, and H. D. Brody

for Contract Period
October 1, 1965 - September 30, 1966

October 1, 1967

Department of Metallurgy
Massachusetts Institute of Technology
Cambridge, Mass. 02139

Contract No. DA-19-020-AMC-5443 (X)
D/A Project No. 1C024401A328
AMCMS CODE 5025.11.294

Metals Research for Army Materiel

Distribution of this Document is unlimited

Army Materials and Mechanics Research Center
Watertown, Massachusetts 02172

ABSTRACT

Analytical and experimental work on microsegregation and dendrite structure in a series of iron base alloys is summarized. Experimental work is on iron-nickel alloys, iron-4% phosphorous alloy, iron-25% copper alloy, and iron-nickel carbon alloys.

A new computer analysis for microsegregation is presented, with detailed numerical results given for iron-26% nickel alloy, iron-10% nickel alloy, and iron-4% phosphorous alloy. Results agree reasonably well with experiment provided the dendrite arm spacing used in calculation is less by a constant "correction factor", g , than that measured (for example $g \approx 0.40$ for cylinder model, secondary dendrite arm spacing). It is concluded the need for the correction factor arises primarily because the model employed for calculation does not account for "ripening" during solidification.

Structures of the various alloys studied are presented; in some, the dendrite morphology is strongly plate-like; in others, it is "fibrous". Over a range of cooling rates from $10^{-3}^{\circ}\text{C/sec}$ to nearly 10^6°C/sec dendrite arm spacing of iron-26% nickel alloy is linearly related to a single power of cooling rate. It is concluded that the dependency results from the predominant effect of "coarsening" in determining final dendrite arm spacing.

TABLE OF CONTENTS

<u>Chapter Number</u>		<u>Page Number</u>
	ABSTRACT	i
	LIST OF FIGURES	iv
	LIST OF TABLES	vii
1	INTRODUCTION	1
	References	4
2	ANALYSES OF MICROSEGREGATION IN BINARY IRON-BASE ALLOYS	5
	A. Summary of Analyses Employed	5
	Method I: Analytic Solution	6
	Method II: Numerical Analysis	8
	Method III: Mass Balance and Finite Difference	9
	B. Alloy System and Diffusion Data Used as Examples	11
	C. Results of Calculations, Iron-26% Nickel Alloy	12
	Method I	12
	Method II	13
	Method III	13
	D. Results of Calculations - Iron-10% Nickel Alloy	15
	E. Results of Calculations - Iron-4% Phosphorus Alloy	15
	F. Conclusions	16
	References	18
3	CASTING PREPARATION AND THERMAL ANALYSIS	30
	A. Unidirectionally Solidified Plate Castings	30
	B. Other Castings	33
	1. Furnace-cooled iron-26% nickel alloy	33
	2. "Splat-cooled" iron-26% nickel alloy	33
	References	35

<u>Chapter Number</u>		<u>Page Number</u>
4	MORPHOLOGY AND DENDRITE ARM SPACING. . .	39
	A. Morphology	39
	B. Dendrite Arm Spacing	40
	C. Discussion	41
	D. Conclusions	44
	References	45
5	MICROSEGREGATION	57
	A. Procedure	57
	B. Iron-nickel Binary Alloys	57
	C. Iron-nickel-carbon Alloys	59
	D. Iron-4% Phosphorous Alloy	60
	E. Discussion	60
	F. Conclusions	62
	References	64
	APPENDIX A: List of Symbols	75
	APPENDIX B: Method III - Finite Difference. Mass Balance Technique	77
	DISTRIBUTION LIST	88

LIST OF ILLUSTRATIONS

<u>Figure Number</u>		<u>Page Number</u>
2-1	Iron-nickel phase diagram	19
2-2	Iron-phosphorus phase diagram	20
2-3	Composition of the solid at the liquid-solid interface, C_s^* as a function of the fraction solid, f_s , for equilibrium, non-equilibrium and several intermediate cases for an iron-26% nickel alloy. Plate model. Method I	21
2-4	Predicted solute distribution at the solidus temperature for an iron-26% nickel alloy with $\eta = 4 \times 10^6$ for different geometries. Method III . . .	22
2-5	Predicted segregation ratios at the solidus, S' , versus η for iron-26% nickel alloy. Plate model	23
2-6	Predicted maximum and minimum solute contents as a function of η for an iron-26% nickel alloy at the solidus and at room temperature. Plate model. Method III	24
2-7	Predicted values of the segregation ratio at the solidus, S' , and at room temperature, S° , as a function of η for iron-26% nickel alloy. Method III	25
2-8	Predicted maximum and minimum solute contents as a function of η for iron-10% nickel alloy at the solidus and at room temperature. Plate model. Method III .	26
2-9	Predicted values of the segregation ratio at the solidus, S' , and at room temperature, S° , as a function of η for iron-10% nickel alloy. Method III	27
2-10	Weight per cent eutectic versus η for an iron-4% phosphorus alloy. Plate model. Method III	28

<u>Figure Number</u>		<u>Page Number</u>
2-11	Minimum solute content at room temperature, C_m , for an iron-4% phosphorus alloy. Plate model. Method III	29
3-1	Schematic diagram of plate model	37
3-2	Cooling curves from the unidirectionally solidified ingot with thermocouples at 1.13, 2.17, 3.15, 4.17, 5.36, and 6.53 inches from the chill	38
4-1	Iron-26% nickel alloy. Photomicrographs at 1", 2", and 4" from the chill. 7.6X .	48
4-2	Iron-26% nickel alloy. Photomicrographs at 1", 2", and 4" from the chill. 34X .	49
4-3	Iron-nickel alloys containing 10% to 26% nickel. Photomicrographs at 2" from the chill. 34X	50
4-4	Iron-26% nickel alloys containing 0% carbon to 0.42% carbon. Photomicrographs at 2" from the chill. 34X	51
4-5	Iron-4% phosphorus alloy. Photomicrographs at 1", 2", and 4" from the chill. 34X	52
4-6	Iron-25% copper alloy. Photomicrographs at 1", 2", and 4" from the chill. 64X .	53
4-7	Dendrite arm spacing versus cooling rate, iron-26% nickel alloy. Furnace cooled data from Mollard ³ . Splat cooled data from Strachan ⁴	54
4-8	Three-dimensional view of iron-26% nickel sample furnace cooled at $4.3 \times 10^{-3}^{\circ}\text{C/sec}$	55
4-9	Two splat cooled samples, iron-26% nickel alloy ⁴ . Top - $2 \times 10^6^{\circ}\text{C/sec}$ cooling rate, 1000X. Bottom - $2 \times 10^5^{\circ}\text{C/sec}$ cooling rate, 500X	56

<u>Figure Number</u>		<u>Page Number</u>
B-1	Schematic diagram of the sequence of steps in the Mass Balance Technique for calculating solute redistribution in an alloy solidifying into a single solid phase of variable composition . . .	86
B-2	Master cooling curve for iron-nickel alloys	87

LIST OF TABLES

<u>Table Number</u>		<u>Page Number</u>
3-1	Chemical Analyses of Ingots Studied . . .	36
4-1	Experimental Data on Cooling Rates and Dendrite Arm Spacings, Iron-26% Nickel Alloy	47
5-1	Furnace Cooled Iron-25% Nickel Alloy . . .	65
5-2	Segregation Ratio in Interrupted Cooling Experiments	66
5-3	Electron Probe Microanalyzer Results . . .	67
5-4	Measured Dendrite Arm Spacing and Solidification Times in Iron-Nickel Alloys	68
5-5	Comparison of Measured and Calculated Segregation Ratios in Iron-Nickel Alloys	69
5-6	The Effect of Carbon on Microsegregation in an Iron-26% Nickel Alloy - 2 Inches from the Chill	70
5-7	Volume Per Cent Eutectic Measured Metallographically at Different Distances from the Chill	71
5-8	Measured Dendrite Arm Spacings and Solidification Time in Iron-4% Phosphorous Alloy	72
5-9	Comparison of Measured and Calculated Weight Per Cent Eutectic in Iron-4% Phosphorous Alloy	73
5-10	Electron Microprobe Analysis for Minimum Phosphorus Contents at Different Distances from the Chill . . .	74

CHAPTER I - INTRODUCTION

Research has been conducted at Massachusetts Institute of Technology on microsegregation in iron-base alloys since late 1962. Results have been summarized in annual reports¹⁻⁴ and portions have been abstracted and published as technical papers⁵⁻⁷; a series of technical papers are now being prepared covering the later work.

General aim of the program has been to obtain a sound engineering understanding of factors influencing the form and distribution of microsegregation in cast steel. Specific aspects of the work have included:

1. Study of dendrite morphology and dendrite arm spacing in iron-base alloys.
2. Analytical and experimental studies on solute distribution (microsegregation) in binary iron-base alloys.
3. Analytical and experimental studies on solute distribution (microsegregation) in ternary iron-base alloys.
4. Analytical and experimental studies on homogenization kinetics in iron-base alloys.

This report summarizes the last part of research in this program devoted primarily to study of solidification of the primary (dendrite) phase in iron-base alloys. Current and planned research deals primarily with second phases. Present

studies emphasize the formation, distribution, and morphology of second phases (especially non-metallic inclusions) precipitating during solidification.

Chapter 2 of this report summarizes results of computer studies on microsegregation in two different binary alloy systems. Iron-nickel was chosen as an example of a system in which essentially complete solid solubility is obtained, and iron-phosphorous as an example of a system containing a eutectic. Portions of the work on iron-nickel were presented earlier³, but the bulk of this chapter deals with results of a new computer analysis of microsegregation.

Chapter 3 summarizes briefly the melting and casting procedures used in experimental portions of this work and Chapter 4 presents results of studies on dendrite morphology and dendrite arm spacing measurements. Again, portions of earlier work on iron-nickel are presented in condensed form for continuity, but most of the work is new including the important correlation of Figure 4-7 which shows that dendrite arm spacing is linearly related to a single power of cooling rate in iron-25% nickel alloy over at least a range of cooling rates from $10^{-3}^{\circ}\text{C/sec}$ to 10^6°C/sec . The former rate was obtained in a controlled cooling furnace and the latter in a "splat cooling" apparatus. Intermediate cooling rates were obtained in unidirectionally solidified ingots. Reasons for the dependency of dendrite arm spacing on cooling rate are discussed.

Chapter 5 summarizes measurements of microsegregation made in binary iron-base alloys over the last several years and compares these measurements with the predictions of the new computer analysis of Chapter 2.

References

1. "Investigation of Solidification of High Strength Steel Castings", M.I.T. Interim Report, Contract No. DA-19-020-ORD-5443, Army Materials Research Agency, 1962.
2. "Investigation of Solidification of High Strength Steel Castings", M.I.T., Interim Report, Contract No. DA-19-020-ORD-5443(X), Army Materials Research Agency, October, 1963.
3. R. V. Barone, H. D. Brody, M. C. Flemings, "Investigation of Solidification of High Strength Steel Castings", M.I.T., Interim Report, Contract No. DA-19-020-ORD-5443(X), Army Materials Research Agency, 30 September 1964.
4. D. Poirier, M. C. Flemings, "Investigation of Solidification of High Strength Steel Castings", M.I.T., Interim Report, Contract No. DA-19-020-ORD-5443(X), October, 1965.
5. M. C. Flemings, "Microsegregation in Castings and Ingots", Hoyt Memorial Lecture, Trans. A.F.S., v. 72, 1964, pp. 353-362.
6. T. Z. Kattamis, M. C. Flemings, "Dendrite Morphology, Microsegregation and Homogenization of Low Alloy Steels", Trans. A.I.M.E., v. 233, 1965, pp. 992-999.
7. M. C. Flemings, "Controlled Solidification", Proceedings of the Twelfth Sagamore Army Materials Research Conference, Strengthening Mechanisms, J. Burke, N. Reed, V. Weiss, Editors. Syracuse University Press, 1966.

CHAPTER 2 - ANALYSES OF MICROSEGREGATION
IN BINARY IRON-BASE ALLOYS

A. Summary of Analyses Employed

In this section, a summary is given of three methods employed for calculation of microsegregation in binary iron-base alloys. The first two of these were developed in an earlier research period and reported elsewhere^{1,2}. A new method of analysis was developed in this work with the aims of (1) treating extensive diffusion in the solid with greater accuracy, and (2) treating the case of cylindrical dendrite geometry.

Computations are for a local characteristic volume element. Assumptions of all methods of analysis employed include the following:¹

1. There is negligible undercooling before nucleation, or from curvature or kinetic effects.
2. There is no mass flow in or out of the volume element considered. Such flow might occur, for example, from movement of liquid by convection or to feed shrinkage, from movement of solid during solidification, or from diffusion.
3. Diffusion in the liquid within the volume element considered is complete.
4. The equilibrium partition ratio, k , applies at the interface.

The three methods of calculating microsegregation are summarized below and their differences highlighted.

Method I: Analytic Solution

For the solidification model described by the above conditions, the redistribution of solute during solidification initially was described analytically by making the following assumptions:

1. The dendrite model is platelike.
2. The rate of advance of the interface is either linear or parabolic.

$$\text{Linear: } \lambda_i \propto t \text{ and } \frac{d\lambda_i}{dt} = \text{constant} \quad (2-1)*$$

$$\text{Parabolic: } \lambda_i \propto \sqrt{t} \text{ and } \frac{d\lambda_i}{dt} = \frac{\text{constant}}{\sqrt{t}} \quad (2-2)$$

3. Diffusion in the solid is sufficiently small that the diffusion does not affect significantly the composition in the solid at the interface

$$\left(\frac{dc_s}{d\lambda} \right)_{\lambda = \lambda_i} = \frac{dc_s^*}{d\lambda_i} \quad (2-3)$$

Now the differential materials balance

$$d(f_L c_L) + d(f_s c_s) = 0 \quad (2-4)$$

is evaluated for the above assumptions using the requirement that the total amount of solute entering the solid due to diffusion in the solid is equal to the diffusion flux at the interface. Then

* Symbols used in the text are defined in Appendix A.

$$\frac{d\lambda_i}{d\theta} = \text{constant } (C_L - C_s^*) df_s = \alpha dC_s^* + (1-f_s) dC_L \quad (2-5)$$

$$\frac{d\lambda_i}{d\theta} = \frac{\text{constant}}{\sqrt{\theta}} (C_L - C_s^*) df_s = 2\alpha f_s dC_s^* + (1-f_s) dC_L \quad (2-6)$$

where

$$\alpha = \frac{D_s t_f}{L^2} \quad (2-7)$$

For constant partition ratio, k , and constant solid diffusion coefficient, D_s , the differential equations (2-5) and (2-6) are easily integrated to obtain simple analytic solutions. For the more general case of variable k and D_s , the differential equations (2-5) and (2-6) are solved numerically. During the isothermal solidification that may occur at the eutectic temperature, solid diffusion diminishes the amount of material of eutectic composition. Method I may be used to compute the change at the eutectic temperature in the eutectic fraction. Method I, however, has not been applied to the solute redistribution that occurs during cooling after solidification.

Method I overestimates the amount of solid diffusion and, thus, underestimates the extent of microsegregation. Errors become serious when αk approaches 1. Finally Method I predicts solid composition at the solid liquid interface, C_s^* , but does not yield a description of the solute distribution within the dendrite.

Method II: Numerical Analysis

To account for solid diffusion after solidification and to achieve a complete description of the solute distribution within the dendrite both during and after solidification, a simple numerical method was employed. For Method II

- (1) The dendrites again are considered platelike
- (2) The rate of advance of the interface is either linear or parabolic (equations 2-5 and 2-6)
- (3) The solid composition at the liquid solid interface, C_s^* , at a particular fraction solid, f_s , is obtained by Method I.

To evaluate solid diffusion during solidification Fick's second law of diffusion is transformed by finite differences to the approximate expression

$$C_{s,j,k} = \frac{C_{s,j+1,k-1} + C_{s,j,k-1} (M - 2) + C_{s,j-1,k-1}}{M} \quad (2-8)$$

where $M = \frac{\Delta \lambda^2}{D_s \Delta t}$ (2-9)

This equation is evaluated iteratively over distance (from $\lambda = 0$ to λ_i) and over time (from $t = 0$ to t_f) for the initial and boundary conditions

when $t = 0$, $\lambda_i = 0$ and $C_s(\lambda_i) = kC_o$

at $\lambda = 0$, $\frac{\partial C_s}{\partial \lambda} = 0$ and at $\lambda = \lambda_i$, $C_s(\lambda_i) = C_s^*$ (2-10)

where C_s^* is given by the Method I for $f_s = \frac{\lambda_i}{L}$.

Method II, also, may be used to calculate the changes in microsegregation at the eutectic temperature. In addition, Method II is readily applied to the computation of the solute redistribution on cooling after solidification by iteratively evaluating equation (2-8) using as the initial condition the solute distribution at the actual solidus temperature and with the boundary conditions for a eutectic alloy:

$$\text{at } \lambda_i = 0, \frac{\partial C_s}{\partial \lambda} = 0; \text{ and at } \lambda = \lambda_i, C_s(\lambda_i) = C_s(\text{max. solubility}) \dots \quad (2-11)$$

and for a single phase alloy:

$$\text{at } \lambda_i = 0, \frac{\partial C_s}{\partial \lambda} = 0; \text{ and at } \lambda = \lambda_i, \frac{\partial C_s}{\partial \lambda} = 0 \quad (2-12)$$

Method II is more accurate than Method I, yet because it depends on the results of Method I for interface composition, it cannot be used when there is a large amount of solid diffusion. Method II underestimates the amount of solid diffusion and solute mass is not conserved. Use of a correction factor described previously², fortuitously, allows the accurate use of Method II for large amounts of solid diffusion. However, the modified method is not straightforward and is time consuming.

Method III: Mass Balance and Finite Difference

Method III is the new numerical technique and computer program that has been developed to account readily for large amounts of solid diffusion and to allow for a variation of dendrite geometry. In this method:

- (1) The dendrite model may be taken as platelike, cylindrical, or spherical.
- (2) The rate of advance of the interface may be linear, parabolic or governed by thermal data.
- (3) The composition in the solid at the interface is set equal to kC_L where C_L is determined by mass balances after every interval of solidification.

Briefly, diffusion within the dendrite is computed using the finite difference technique, i.e. by iteratively evaluating the algorithm (2-8) for $0 < \lambda < \lambda_i$. Then the mass balance, equation (2-4), is used to compute the new composition of the liquid. An amount $\Delta\lambda$ of solid is considered to form at the composition that is in equilibrium with the liquid, kC_L , and the process is repeated. This method may also be used to compute solute redistribution at the eutectic transformation and on cooling after solidification. The details of the numerical method are given in Appendix B.

In summary, Method III is a straightforward technique readily used to describe solute distribution within a dendrite during solidification and on cooling after solidification. The method is accurate even for large amounts of solid diffusion and may be used for cylindrical as well as platelike dendrite geometrics.

B. Alloy Systems and Diffusion Data Used as Examples

Two binary alloy systems were used in this study as examples for calculation. The first of these is the iron-nickel system. In this system alloys above about 6 per cent nickel solidify completely as a single phase, austenite. In all iron-nickel alloys, the composition of interdendritic spaces is expected to approach, as a limit, the composition of the liquidus minimum at 68% nickel, Figure 2-1. The second alloy system used as example is the iron-phosphorous system, which has a simple eutectic at the iron-rich end with limited solid solubility, Figure 2-2.

Data for the diffusion coefficient used in calculations for iron-nickel alloys are from Goldstein³ who showed the diffusion coefficient for the γ phase varies with both temperature and nickel content according to the relation,*

$$D_s = \exp [0.0519 X_{Ni} + 1.51] \exp \left[- \frac{38,380 - 5.85 X_{Ni}}{T} \right] \quad (2-13)$$

where X_{Ni} = atomic per cent nickel

T = temperature, degrees, Kelvin

Data for the diffusion coefficient used in the calculations for the iron-phosphorus system were taken from Seibel⁴ who

* Goldstein reports the above expression to be in agreement with his measured values of D_s within ten per cent for nickel contents up to 50 per cent in the temperature range of 1000°C to 1288°C. In the work equation (2-1) is employed for compositions up to 68 per cent nickel and in the temperature ranges 800°C to 1469.5°C.

lists the following expression for phosphorus diffusion in α :

$$D_s = 2.90 \exp \left[-\frac{55000}{RT} \right] \quad (2-14)$$

where R = gas constant.

In this work, solutions are presented only for a linear volumetric growth rate and for platelike and cylindrical dendrite geometries.

C. Results of Calculations, Iron-26% Nickel Alloy

Method I:

Details of this analysis (the simplest employed herein) have been given earlier. Results for iron-26% nickel alloy are given in Figure 2-3, which plots solid composition at the interface, C_s^* , versus fraction solid, f_s , for various values of η , where:

$$\eta = \frac{t_f}{L^2} \quad (2-15)$$

At $\eta = 0$, diffusion in the solid is negligible and the calculated curve is that resulting from the Scheil equation (with variable k). At $\eta = \infty$, diffusion in the solid is complete and the result is that obtained from the equilibrium lever rule.

If diffusion in the solid is slight ($\eta \ll 1$), then the curves of Figure 2-3 also represent approximately the solid concentration, C_s , that would be measured from a microprobe trace across the platelike dendrite arms. This trace would

start at the center of the arm ($f_s = 0$) and end at the center plane between the two dendrite arms ($f_s = 1$). It is clear, however, that Figure 2-3 cannot be used in this way as $\eta = \infty$, for example, the interface composition C_s^* is as shown in Figure 2-3. However, the final solid composition, C_s , would be 26% nickel at all values of f_s .

Method II:

This finite difference method (Method II, Appendix A) was employed previously to give a better description of composition across dendrite arms. For substantial diffusion such as is clearly present in iron-26% nickel, this method has been superceded by Method III, the "mass balance technique". Some results of this technique are, however, discussed below for comparison with Method III.

Method III:

Typical results of Method III are given in Figure 2-4. Figure 2-4 shows solid composition, C_s , versus fractional distance, λ/L , along a dendrite arm (after solidification) for a platelike dendrite model, assuming $\eta = 4 \times 10^6$ and linear advance of the solid-liquid interface with time. Also shown in Figure 2-4 are results for the cylindrical dendrite model. Segregation in the cylindrical model is significantly less than that in the plate model. Comparison of Figure 2-4 with 2-3 shows that in the plate model, $\eta = 4 \times 10^6$, results of Methods I and III are closely similar. The results of Method II and

Method III are compared in Figure 2-5 which gives "Segregation Ratios" * at the solidus temperature, S' versus k calculated by Methods II and III (plate model). Segregation ratios at all values of η are closely similar (but slightly less for Method III).*

Figure 2-6 shows local maximum and minimum solute contents at the actual solidus temperature, C_M' and C_m' , plotted individually versus η . Also shown are the local maximum and minimum solute contents at room temperature, C_M° , C_m° . Calculation of room temperature values was based on cooling curve data obtained from unidirectionally solidified ingots as discussed in Chapter 3; and the method of calculation is described in Appendix B. It is evident in Figure 2-6 that the ratio of C_M°/C_m° is substantially less than C_M'/C_m' predicted as a result of diffusion in the solid during cooling.

Figure 2-7 shows the variation of both S' and S° (where $S^\circ = C_M^\circ/C_m^\circ$) with η for plate and cylinder dendrite models.

* Segregation Ratio, S , is defined as:

$$S = \frac{C_M}{C_m}$$

C_M = maximum composition of the solid within regions the order of a dendrite arm spacing

C_m = minimum composition of the solid within regions the order of a dendrite arm spacing

The quantities are primed (S' , C_M' , C_m') when taken at the non-equilibrium solidus temperature and written as S° , C_M° , C_m° when taken at room temperature.

Lowest segregation is for the cylinder model at room temperature.

D. Results of Calculations - Iron-10% Nickel Alloy

Figures 2-8 and 2-9 show summary results of calculations on iron-10% nickel performed similar to the foregoing (Method III). The following general observations may be made from these figures:

- (1) Significant homogenization occurs in this alloy after solidification and during cooling to room temperature for all values of η plotted (as in iron-26% nickel alloy).
- (2) The cylindrical dendrite model predicts less segregation at all values of η than does the platelike model (as in iron-26% nickel alloy).
- (3) Calculated values of S' and S° are significantly higher for iron-10% nickel alloy than for iron-26% nickel alloy.

E. Results of Calculations - Iron-4% Phosphorus Alloy

Figures 2-10 and 2-11 show results of calculations on the iron-phosphorous system (see phase diagram, Figure 2-2). This alloy system contains a eutectic at 10.2% P, and the limit of solid solubility at the eutectic temperature is 2.8%.

Figure 2-10 shows calculated weight per cent eutectic versus η for iron-4.0% phosphorous alloy at the solidus (eutectic)

temperature, and for room temperature. Note the extent of solid state diffusion after solidification is much less in this alloy than in the iron-nickel alloys, primarily because the concentration gradients in the solid are much less.

Figure 2-11 shows how predicted minimum composition (at the center of dendrite arms) should vary with η . This minimum goes from kC_0 at low values of η to the maximum solid solubility (2.8%) at higher values of η .

F. Conclusions

1. A new computer program was written to simulate solidification and post-solidification heat treatments by using numerical analysis techniques. The program may be applied to eutectic alloys as well as those in which (a) the final solidification temperature and composition are variable; and (b) substantial diffusion occurs in the solid both during and after solidification. Characteristics of the program are that (a) it precisely conserves solute mass, (b) it permits assumption of either a cylindrical or platelike dendrite, (c) growth rate in the solidification range may be linear, parabolic, or determined by a cooling curve or cooling expression, (d) any desired cooling curve or cooling expression may be employed from the solidus temperature to room temperature.

2. For values of η (local solidification time divided by the square of half the dendrite arm spacing) that will later be seen to be experimentally obtained for iron-nickel alloys:

(a) Significant diffusion occurs in the solid during solidification.

(b) Significant diffusion occurs in the solid after solidification and during cooling to room temperature.

3. For a given value of η , predicted segregation ratios, S' (at the solidus temperature) and S° (at room temperature) are (a) less for iron-26% nickel than for iron-10% nickel, and (b) less in both alloys for cylindrical model than for the plate model.

4. In iron-phosphorous alloys, residual eutectic and minimum concentration at the centers of dendrite arms depend on η . At a given value of η , extent of diffusion in the solid is much less than for the iron-nickel alloys studied.

References

1. H. D. Brody, M. C. Flemings, "Solute Redistribution in Dendritic Solidification", Trans. AIME, v. 236, 1966, pp. 615-624.
2. R. V. Barone, H. D. Brody, M. C. Flemings, "Investigation of Solidification of High Strength Steel Castings", M.I.T. Interim Report, Contract No. DA-19-020-ORD-5443(X), Army Materials Research Agency, 30 September 1964.
3. J. I. Goldstein, Sc.D. Thesis, Department of Metallurgy, 1964.
4. G. Seibel, "Diffusion du Soufre et du Phosphore dans le Fer a l' Etat Solid", Memoires Scientifiques Rev. Metallurgy, LXI, v. 6, 1964, p. 432.

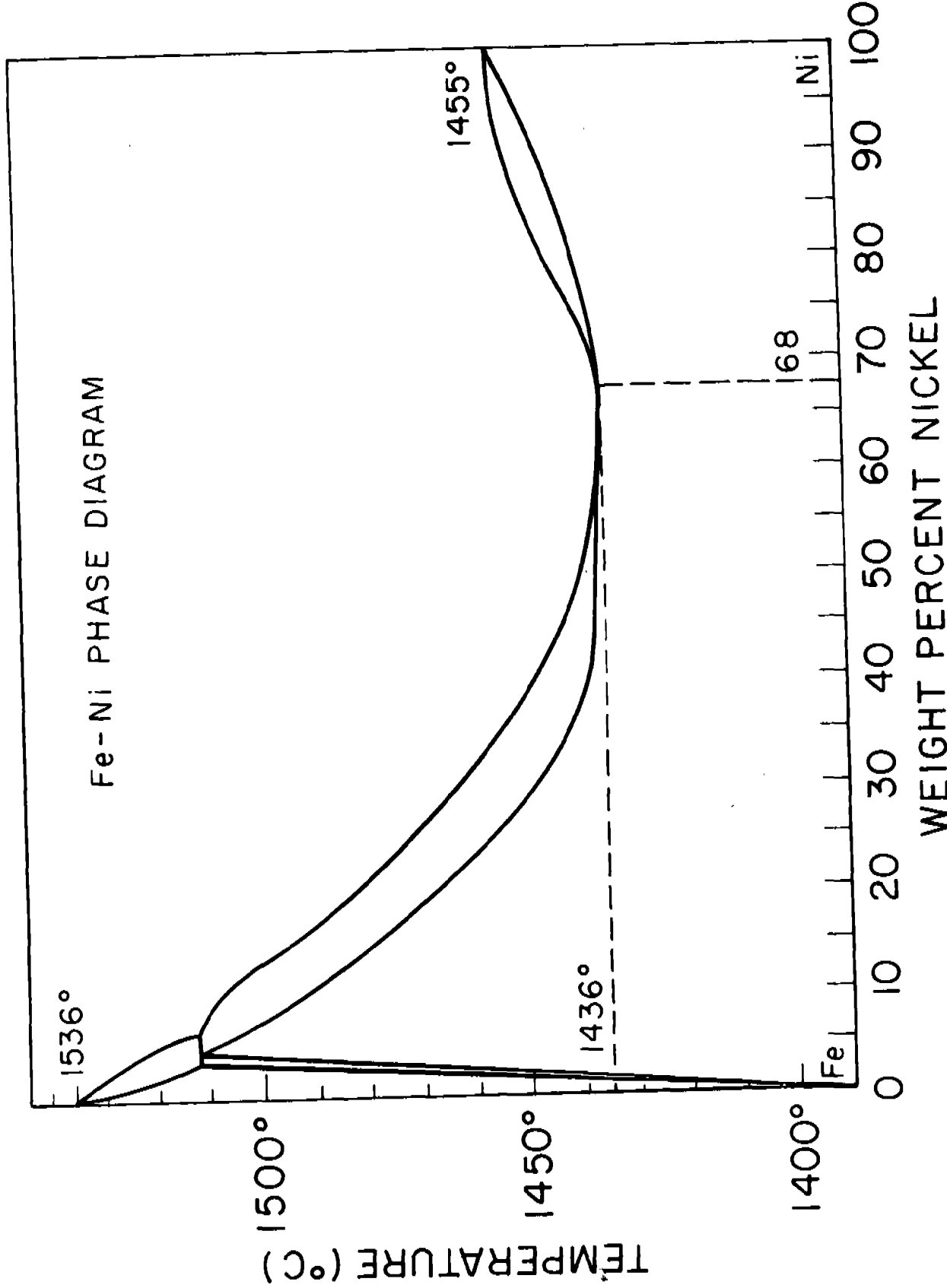


Figure 2-1. Iron-nickel phase diagram

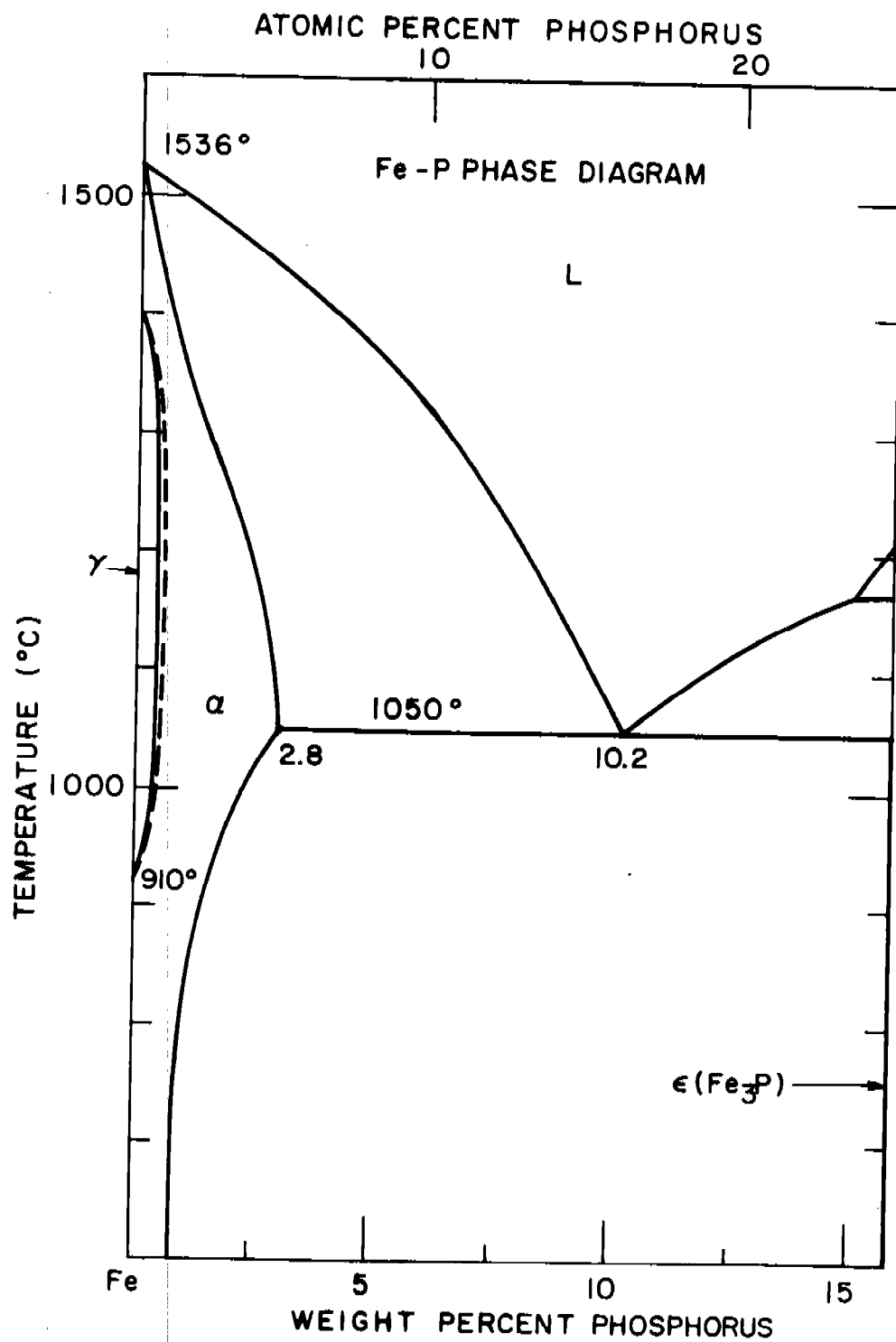


Figure 2-2. Iron-phosphorus phase diagram

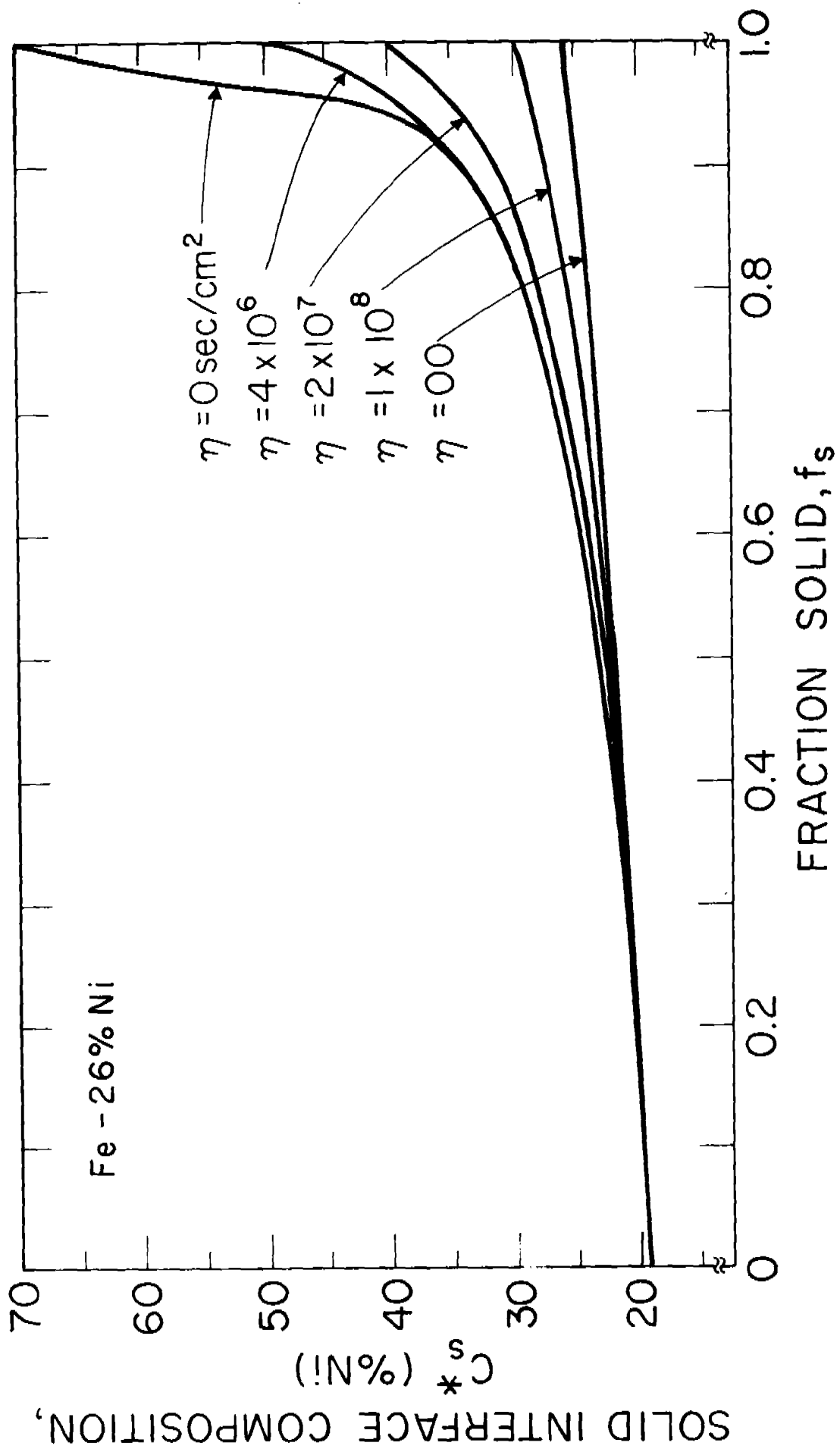


Figure 2-3. Composition of the solid at the liquid-solid interface, C_s^* as a function of the fraction solid, f_s , for equilibrium, nonequilibrium and several intermediate cases for an iron-26 per cent nickel alloy. Plate model. Method I.

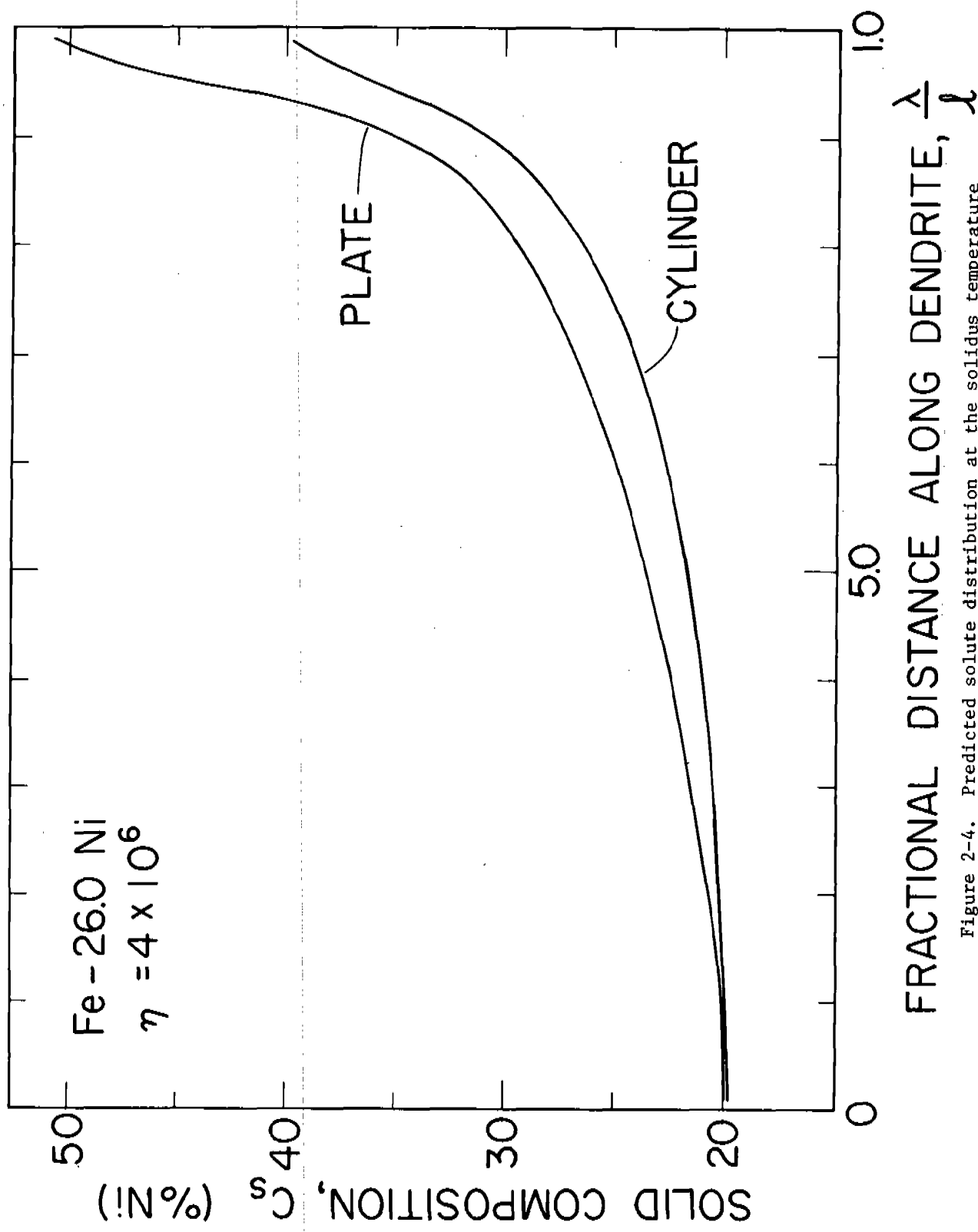


Figure 2-4. Predicted solute distribution at the solidus temperature for an iron-26 per cent nickel alloy with $\eta = 4 \times 10^6$ for different geometries. Method III.

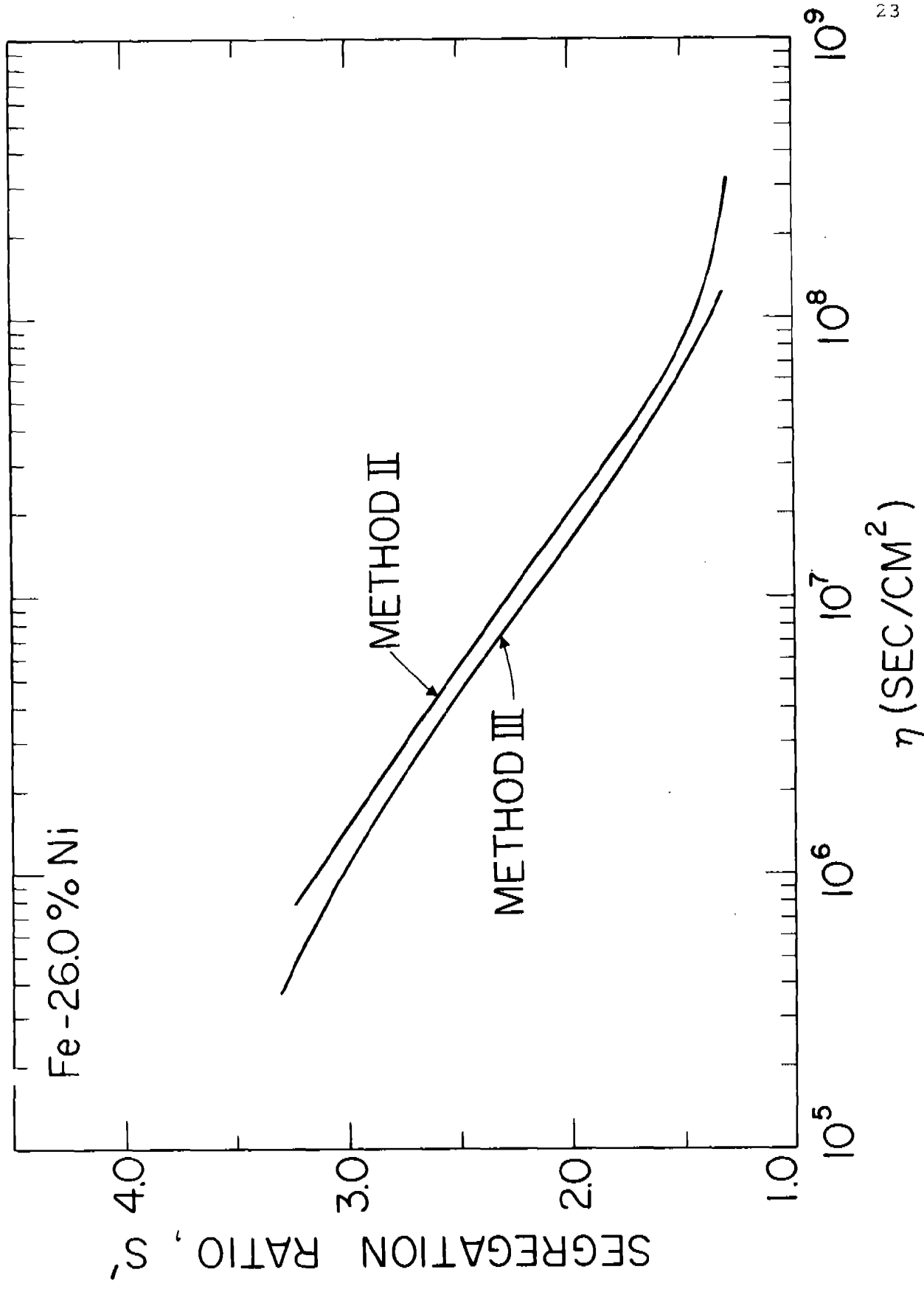


Figure 2-5. Predicted segregation ratios at the solidus, S^1 , versus η for iron-26 per cent nickel alloy. Plate model.

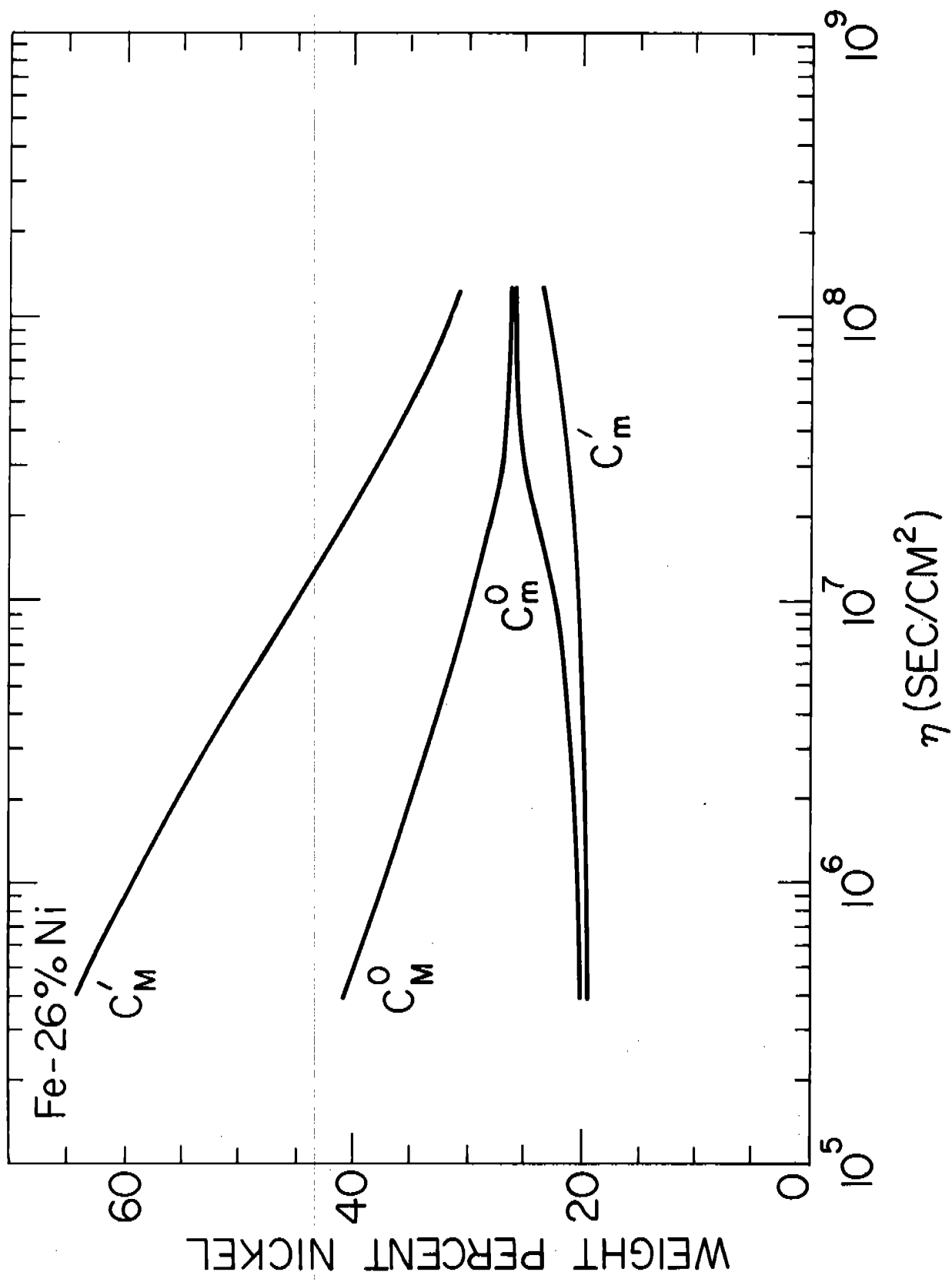


Figure 2-6. Predicted maximum and minimum solute contents as a function of η for an iron-26 per cent nickel alloy at the solidus and at room temperature. Plate model. Method III.

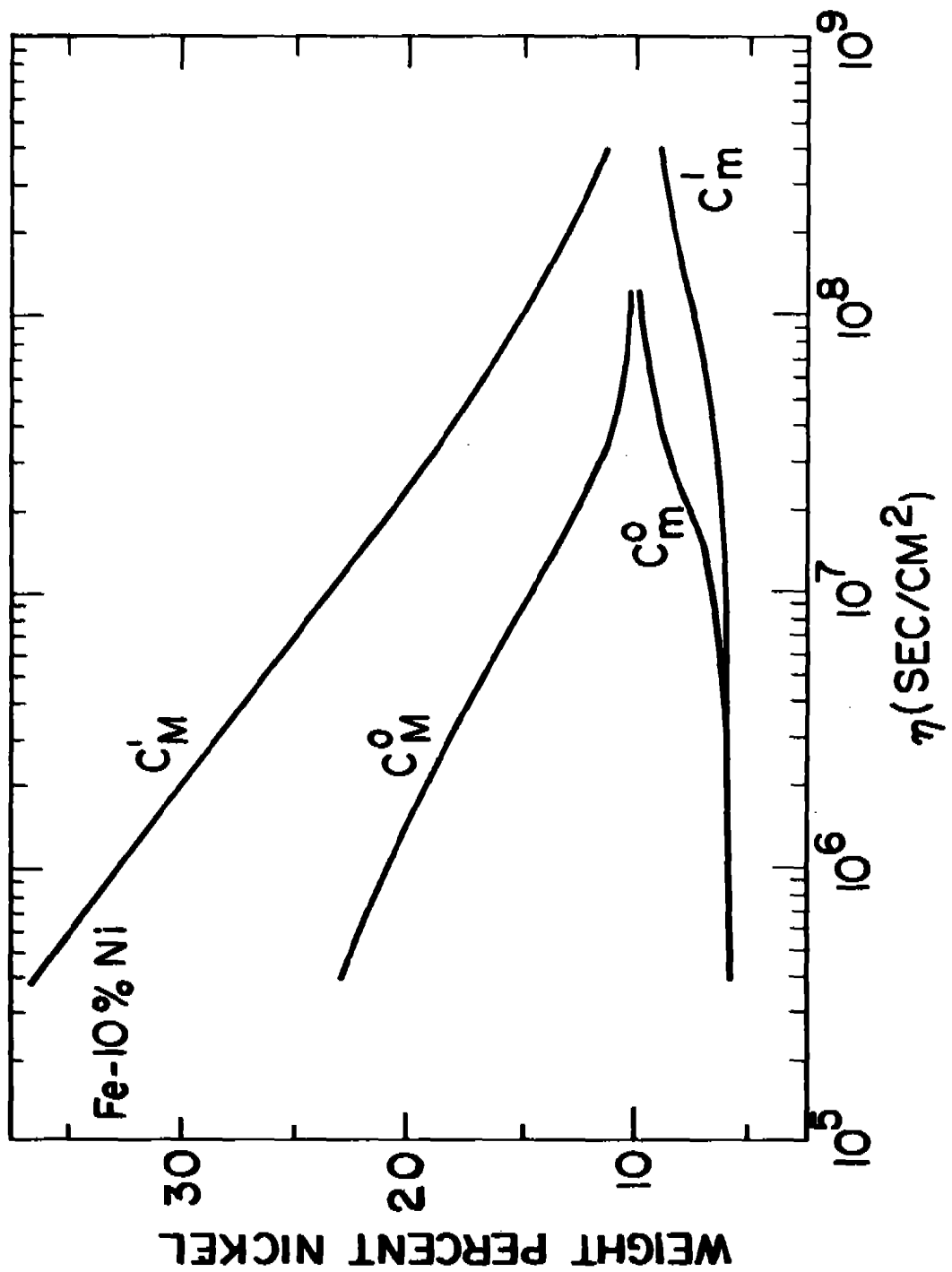


Figure 2-8. Predicted maximum and minimum solute contents as a function of η for iron-10 per cent nickel alloy at the solidus and at room temperature. Plate model. Method III.

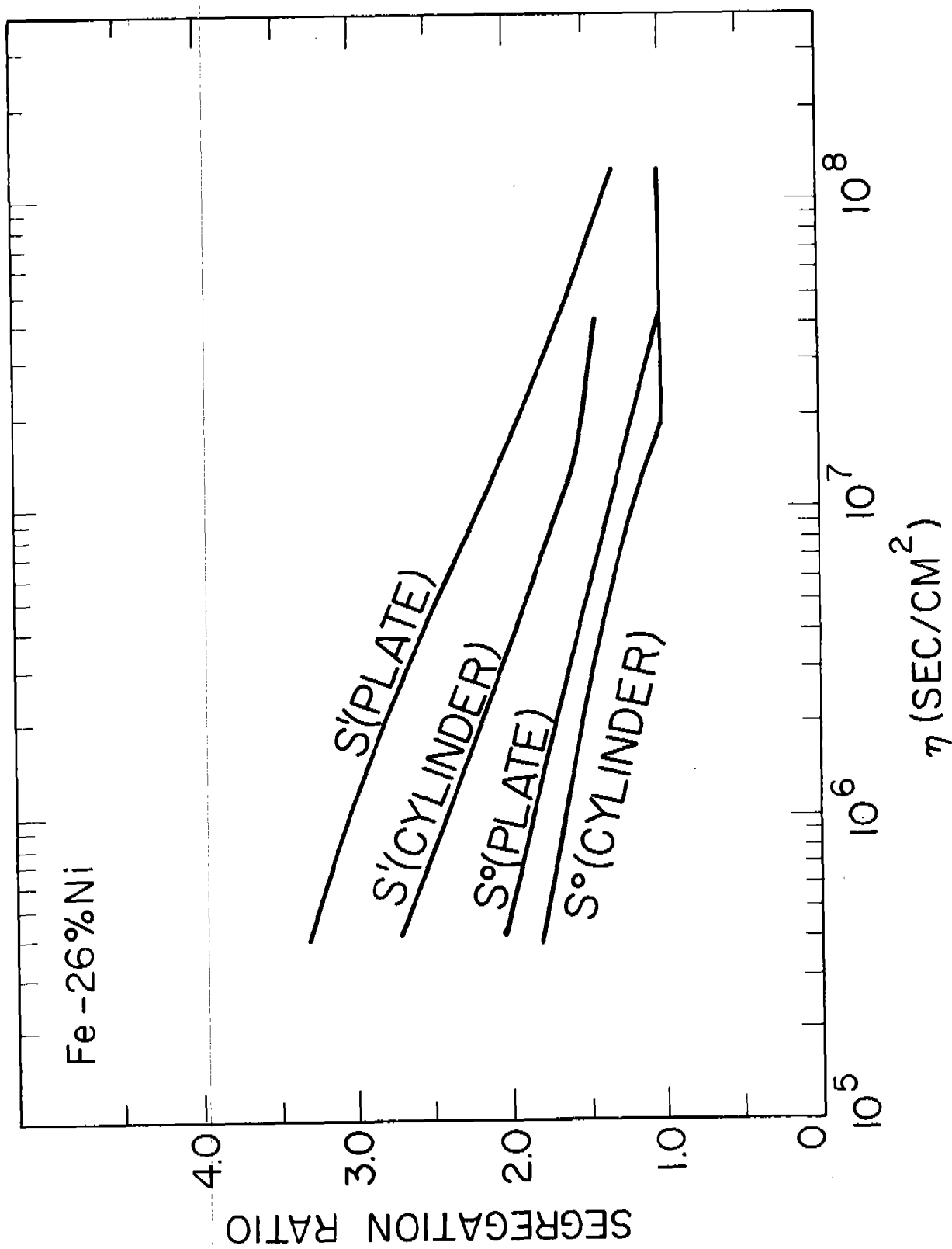


Figure 2-7. Predicted values of the segregation ratio at the solidus, S' , and at room temperature, S° , as a function of η for iron-26 per cent nickel alloy. Method III.

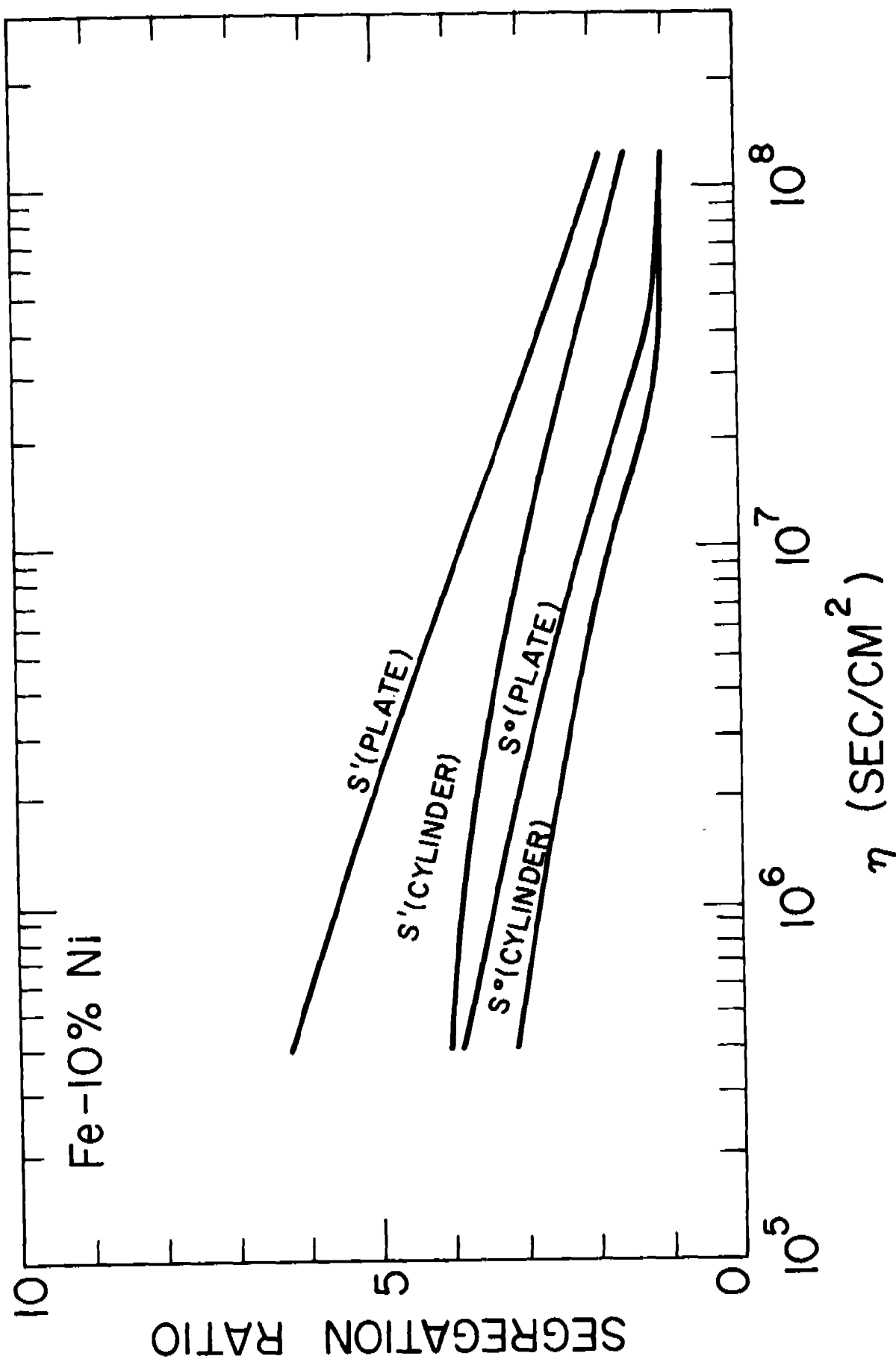


Figure 2-9. Predicted values of the segregation ratio at the solidus, S' , and at room temperature, S° , as a function of η for iron-10 per cent nickel alloy. Method III.

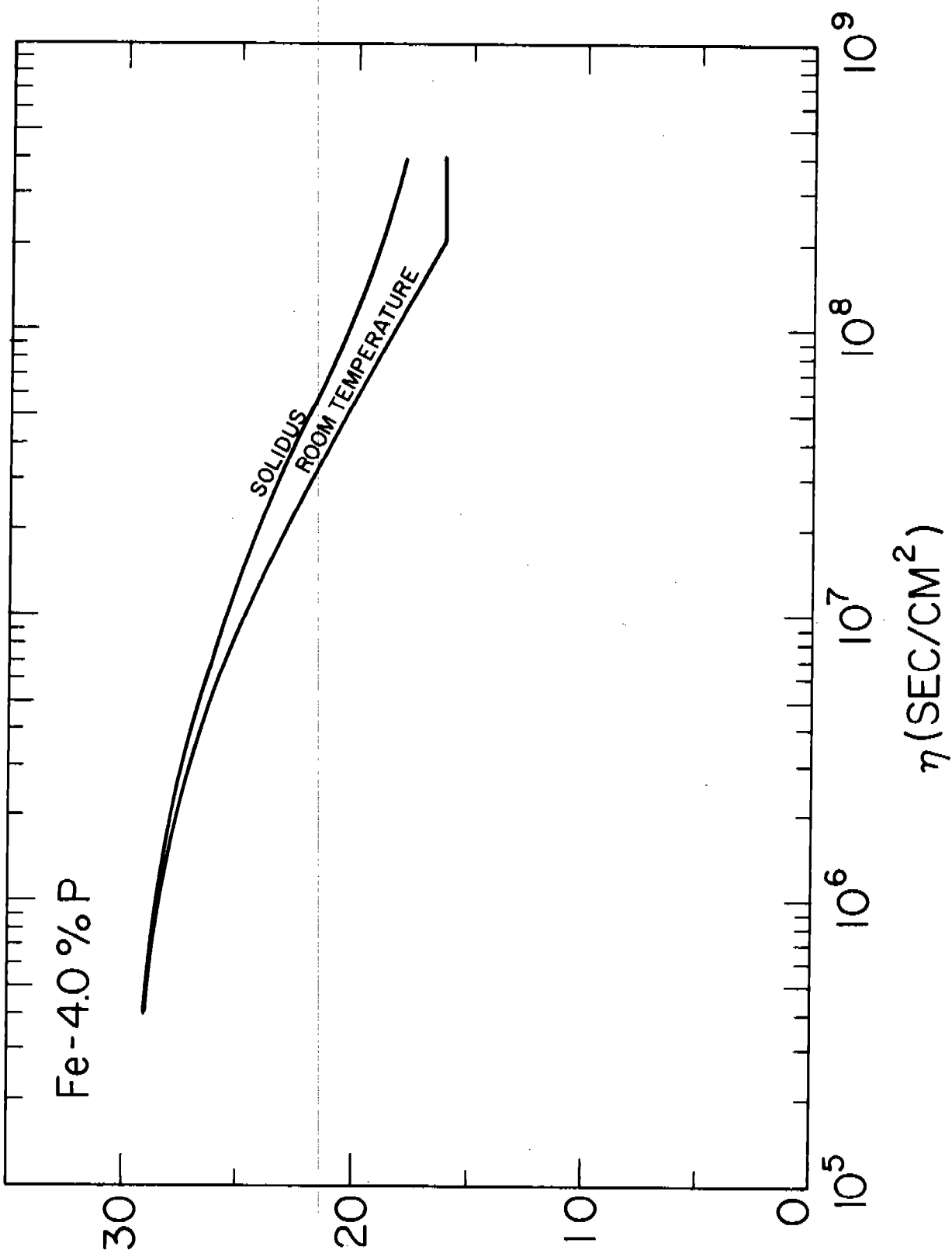


Figure 2-10. Weight per cent eutectic versus η for an iron-4.0 per cent phosphorus alloy. Plate Model. Method III.

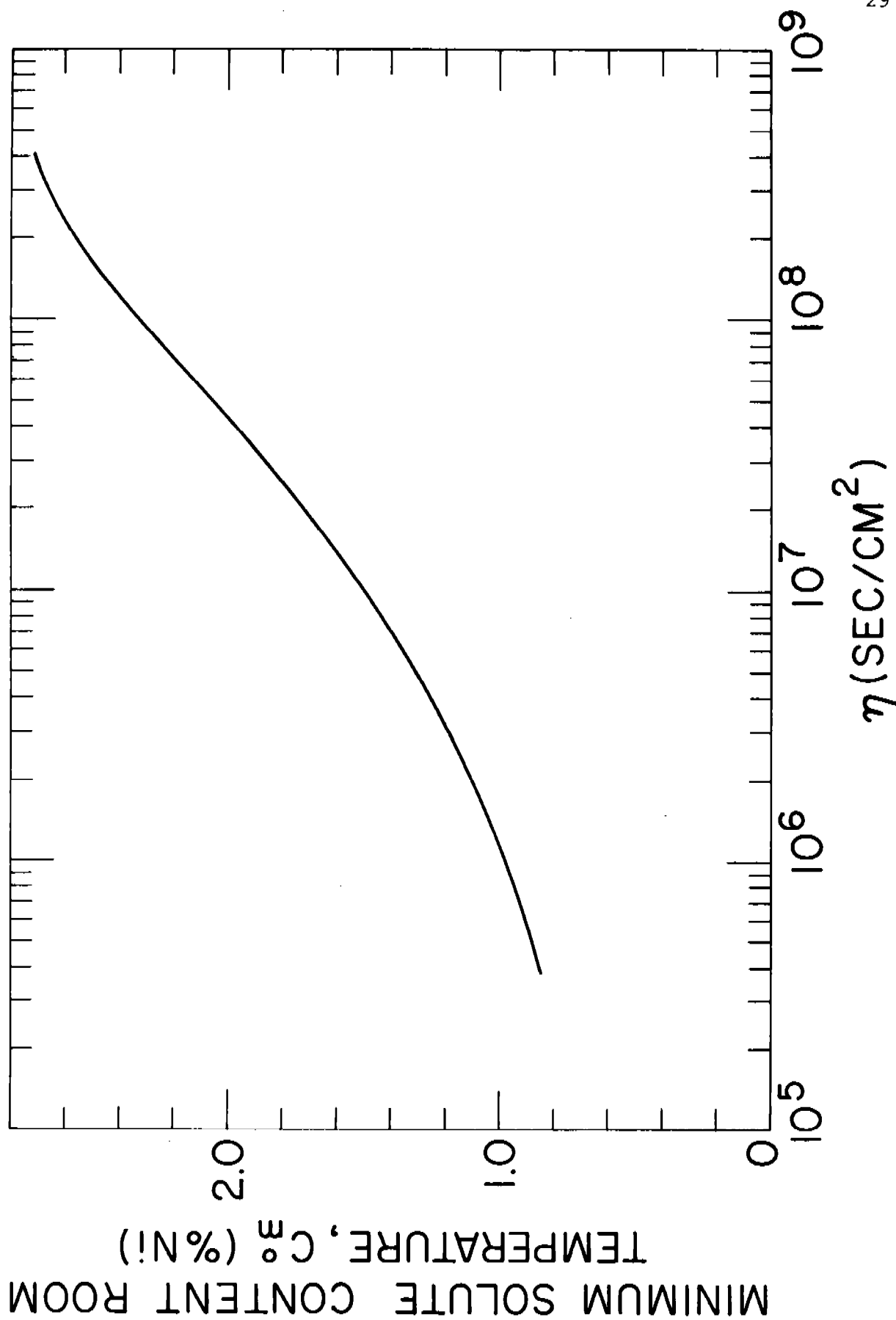


Figure 2-11. Minimum solute content at room temperature, C_m , for an iron-4.0 per cent phosphorous alloy. Plate model. Method III.

CHAPTER 3 - CASTING PREPARATION AND THERMAL ANALYSIS

A. Unidirectionally Solidified Plate Castings

A number of alloys were prepared in the iron-nickel iron-phosphorus, and iron-copper binary systems, and the iron-nickel-carbon ternary system for study of microsegregation and dendrite morphology. A list of the alloys studied, the charge compositions, and the results of chemical analyses are given in Table 3-1.

All heats were induction melted in clay graphite crucibles with rammed linings of magnesite. Melts were deoxidized by additions of 0.5 per cent aluminum. Part or all of the aluminum was added prior to tapping at 3000°F. In all cases the temperature of the melt was measured using an optical pyrometer prior to tapping. No further temperature measurements were made before pouring.

All of the ingots were cast in plate molds 1 inch thick by 5 inches wide by 8 inches high topped by a riser which tapered from 5 inches by 1 inch to 7 inches by 3 inches over a distance of 4 inches. A schematic diagram of this mold is shown in Figure 3-1. The mold was a composite of CO_2 sand and exothermic molding material. The exothermic sleeve was 1/2" thick at the chill and had a 5/24 in/in taper. The exothermic material ignites and heats to a temperature above that of the melting point of steel. Either of two commercial exothermic materials was used: Exomold E or LD Exothermic Material. To avoid gas

pick-up the cope sections were all baked for a minimum of 24 hours at 600°F. The drag portion of the mold consisted of a water cooled copper chill block which was given a light zircon wash and supported by CO₂ sand.

Although the casting weighed 20 pounds, 40 pound heats were always melted in order to improve chemical and temperature control. The iron-phosphorous alloy was melted under argon gas to minimize phosphorous oxidation. All of the heats were skimmed, killed, tapped at 3000°F, and then top poured directly into the mold. The exothermic mold was not ignited before pouring. Hot water was first run through the chill until the molten metal was poured into the mold at which time cold water was used. This procedure prevented condensation on the chill. After filling the mold, the casting was capped with additional exothermic material to reduce top heat loss. Structures of the castings poured were fully columnar, with the columnar grains extending from the chill up into the riser. Typical microstructures are shown later in this report.

Thermal measurements were made during the solidification and cooling rate of one of the iron-26 per cent nickel ingots cast, and reported previously¹. Twenty mil platinum-platinum-10 per cent rhodium thermocouples were inserted horizontally through the exothermic sleeve in the 5-inch direction at distances from the chill of 1 inch, 2 inches, 3 inches, 4 inches, 5 inches and 6 inches. Each thermocouple was protected by 1/16-inch I.D. and 1/8-inch I.D. fused silica tubes. In addition, a 3/16-inch fused

silica protection tube was used where the thermocouple penetrated the exothermic, and a layer of CO_2 sand about $1/4$ -inch thick separated each thermocouple ensemble from the exothermic material. Details of the procedure have been described¹.

Cooling curves measured for the unidirectionally solidified ingot are shown in Figure 3-2. The sharp change in slope of each curve indicates the time the dendrite tips reach the position of the thermocouple (due to the higher thermal conductivity of the solid). It is clear that the solidification front progresses unidirectionally from the chill. The breaks measured at thermocouples 3, 4, 5 and 6 occur at very close to the same temperature, namely 1468°C .

From these curves, the position of any isotherm as a function of time is readily plotted. From such plots, the position of the liquidus and solidus were shown to conform closely to the expressions¹:

$$X_L = .153 \sqrt{t'} - .239 \quad (3-1)$$

$$X_S = .145 \sqrt{t'} - .238 \quad (3-2)$$

where t' = time from pour

where X_L is position of liquidus isotherm (1468°C) at time t' , and X_S is position of solidus isotherm (liquidus minus 25°C)*. Time is in seconds and distance in inches.

* The solidification range clearly must be between the equilibrium range (13°C) and the range for no solid diffusion (32°C). Reasoning backwards from segregation measurements to be reported later, the range must be about 25°C . See, for example, Figure

The "local solidification time", t_f , as a function of distance, is readily calculated from equations (3-1) and (3-2) as:

$$t_f = 4.84 x^2 + 2.22 x + 0.25 \quad (3-3)$$

and averaging cooling rate, ϵ , in $^{\circ}\text{C/sec}$ is 25°C divided by t_f :

$$\epsilon = (.194 x^2 + .089 x + .01)^{-1} \quad (3-4)$$

Cooling rates and dendrite arm spacings at different locations in this ingot are summarized in Table 4-1.

B. Other Castings

To establish relationships between dendrite arm spacing and cooling rate (given in Chapter 4), data were correlated from earlier studies as discussed below.

1. Furnace-cooled iron-26% nickel alloy

Data for this alloy in the cooling rate range of $10^{-3}^{\circ}\text{C/sec}$ to 5°C/sec were obtained by F. R. Mollard and M. C. Flemings in earlier research supported by U.S. Army Materials Research Agency at M.I.T.² (during the period December 9, 1961 to December 8, 1962). These relatively slow cooling rates were obtained in a controlled solidification furnace. The data are summarized in Table 4-1.

2. "Splat-cooled" iron-26% nickel alloy

In a separate study supported by United States Steel Corporation³, small droplets of iron-26% nickel alloy were

levitation melted and then rapidly solidified ("splat-cooled") by dropping them between an electrically actuated "hammer and anvil". Cooling rates were measured by an optical sensor embedded in the stationary platen. Results are summarized in Table 4-1.

References

1. R. V. Barone, H. D. Brody, M. C. Flemings, "Investigation of Solidification of High Strength Steel Castings", M.I.T. Interim Report, Contract No. DA-19-020-ORD-5443(X), Army Materials Research Agency, 30 September 1964.
2. "Investigation of Solidification of High Strength Steel Castings", M.I.T., Interim Report, Contract No. DA-19-020-ORD-5443(X), Army Materials Research Agency, October, 1963.
3. R. W. Strachan, "A Technique for Levitation Melting, Undercooling and Splat Cooling of Metals and Alloys", Ph.D. Thesis, M.I.T., Department of Metallurgy, 1967.

TABLE 3-1
Chemical Analyses of Ingots Studied

Heat Number	Nominal				Actual*				
	% Ni	% C	% Cu	% P	% Ni	% C	% Cu	% P	% Al
1	10.0	-	-	-	9.86	-	-	-	0.06
2	15.0	-	-	-	14.7	-	-	-	0.04
3	20.0	-	-	-	19.9	-	-	-	0.21
4	26.0	-	-	-	26.0	-	-	-	0.24
5	26.0	.12	-	-	25.0	0.12	-	-	0.14
6	26.0	.33	-	-	24.1	0.33	-	-	0.24
7	26.0	.42	-	-	24.6	0.42	-	-	0.18
8	26.0	-	-	-	25.8	-	-	-	0.47
9	-	-	-	4.0	-	-	-	-4	-
10	-	-	25.0	-	-	-	25.0	-	0.005

* Chemical analyses were taken at approximately 1/2 inch from the chill. 0.5 per cent aluminum added as deoxidizer to all heats.

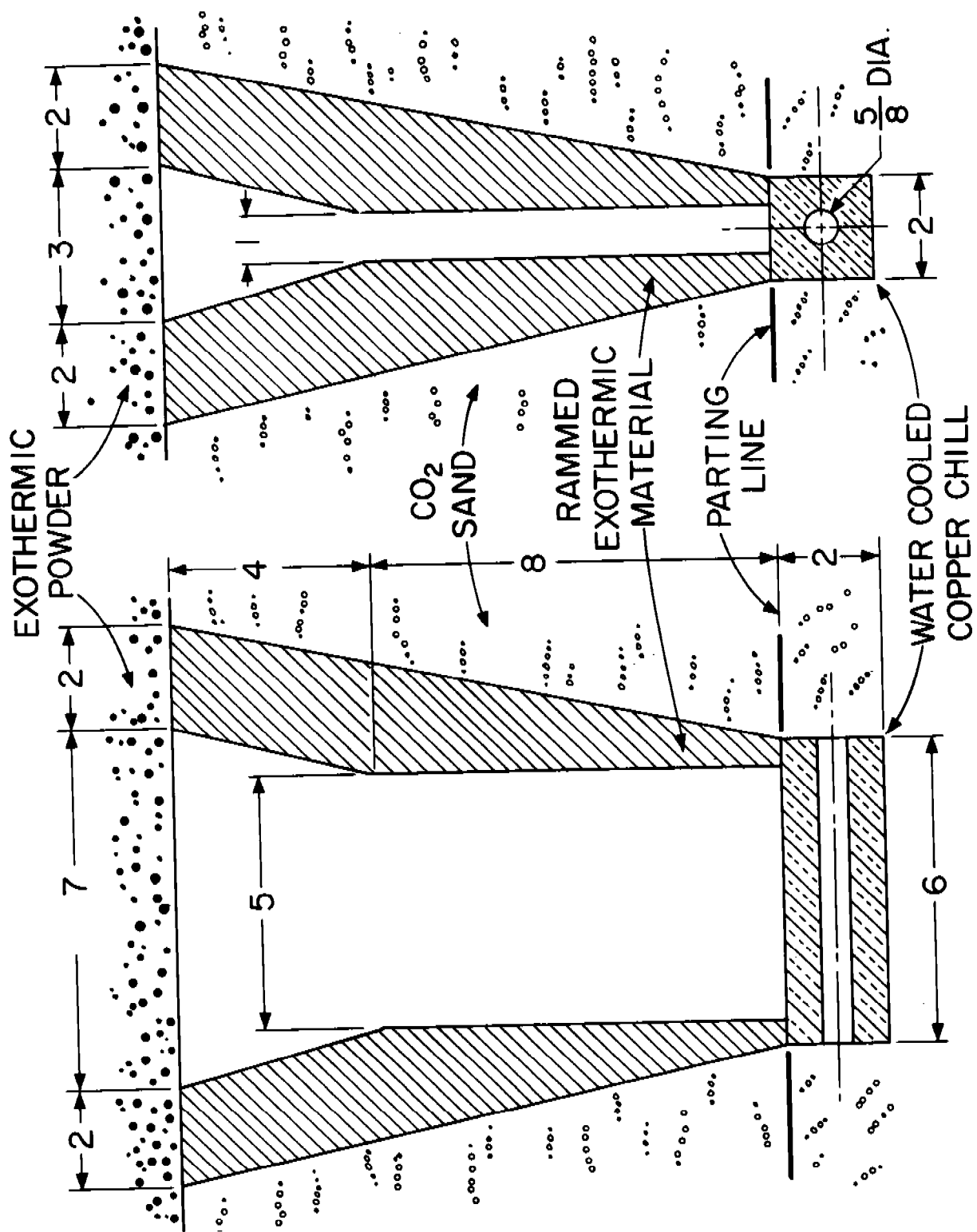


Figure 3-1. Schematic diagram of plate mold.

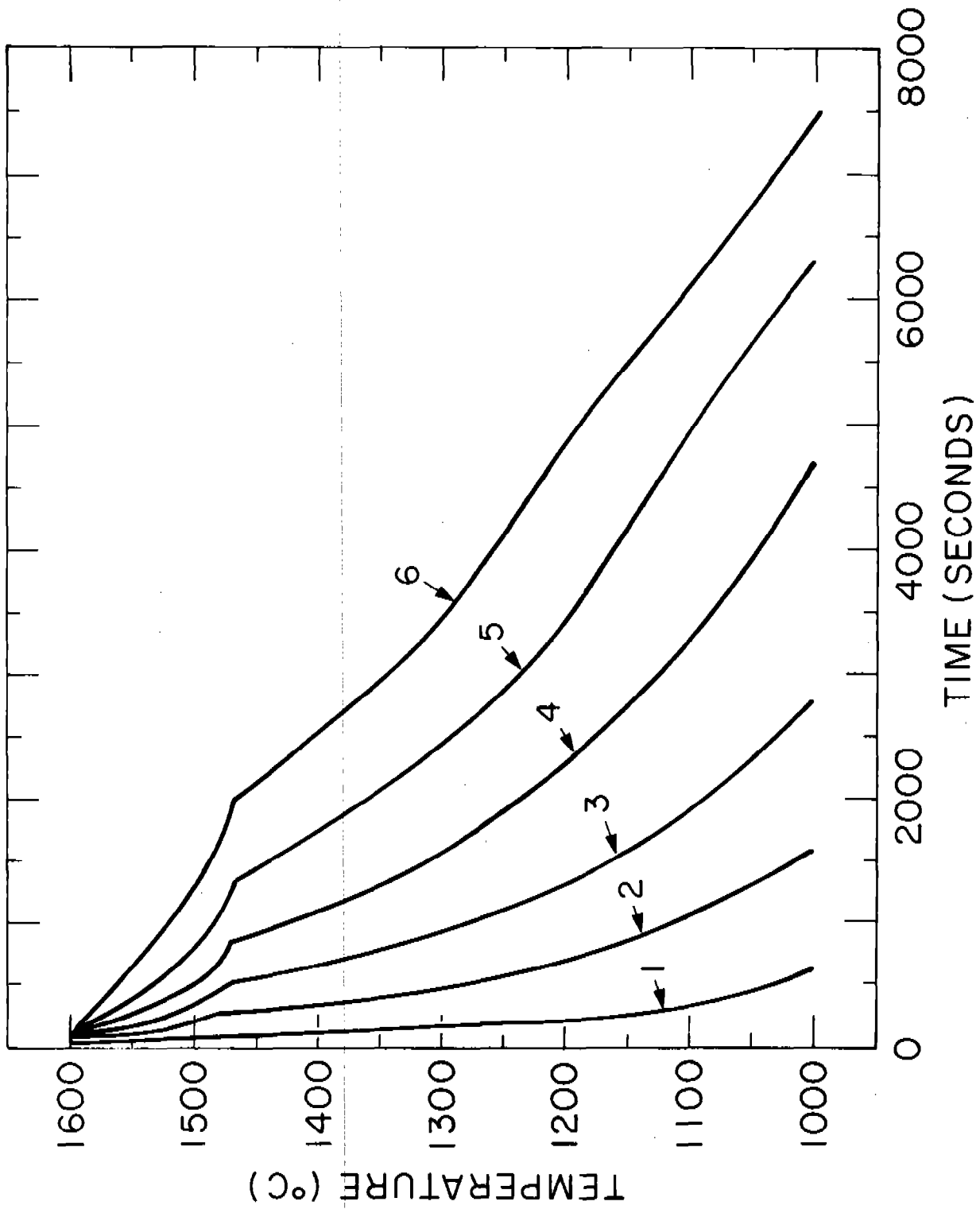


Figure 3-2. Cooling curves from the unidirectionally solidified ingot with thermocouples at 1.13, 2.17, 3.15, 4.17, 5.36, and 6.53 inches from the chill.

CHAPTER 4 - MORPHOLOGY AND DENDRITE ARM SPACINGS

A. Morphology

Figures 4-1 to 4-6 show selected photomicrographs from this study, for iron-nickel, iron-nickel-carbon, iron-phosphorous and iron-copper alloys.

General observations from these photomicrographs are the following:

- (1) The dendrite structures tend to become more fully developed with increasing distance from the chill (and hence with increasing "local solidification time" or "decreasing cooling rate"). Note, for example, the horizontal sections of the iron-26 per cent nickel alloy (Figures 4-1 and 4-2).
- (2) In the iron-nickel alloys, the leaner alloys (10% and 15% nickel) have less fully developed dendrites than the richer alloys. In the transverse sections of Figure 4-3, for example, the lower solute containing alloys appear almost "cellular". We continue to call these dendrites, however, since from orientation of the transformation structure, it is clear that they are growing in the dendrite direction, $<100>$, and use the term "fibrous dendrites" when no side branching is visible.*

* We prefer to distinguish between "cells" and "dendrites", not by presence or absence of secondary dendrite arms, but only by the criterion that the dendrite must grow in or near its crystallographic growth direction.

- (3) Interstices between secondary dendrite arms tend to fill in as previously described to form primary plates (e.g., iron-26% nickel) or continuous "fibrous" shapes (iron-10% nickel, iron-15% nickel).
- (4) Iron-nickel alloys containing carbon are more readily etched than those without carbon and, perhaps partly for this reason, dendrites in the ternary alloys appear better developed than those of the iron-nickel binary (Figure 4-4).
- (5) In iron-4% phosphorous and iron-25% copper alloys, horizontal "secondary plates" develop in addition to (the less direct) primary plates, Figures 4-5 and 4-6.

B. Dendrite Arm Spacing

Qualitative comparison of the structures of Figures 4-1 to 4-6 indicates only modest effect of alloy content on secondary dendrite arm spacing. For example, for a location 2" from the chill, secondary dendrite arm spacings in all alloys studied were between 75 and 90 microns. Detailed measurements of the spacings have been reported^{1,2}.

Alloy analysis influenced primary arm spacing much more than it did secondary arm spacing. For example, in Figure 4-4, note the primary spacings of the alloys containing .12% carbon and .42% carbon are significantly larger than those of the two alloys containing 0% carbon and .33% carbon. Secondary arm spacings are, however, little changed by the change in analysis.

Dendrite arm spacing is strongly influenced by distance from the chill (and hence "local solidification time" or "cooling rate"). To illustrate this, data on iron-26% nickel alloy have been assembled from current and earlier work^{3,4} in Table 4-1 (as described in Chapter 3). These same data are plotted in Figure 4-7 as dendrite arm spacing versus cooling rate. Note that over a range of cooling rates from about $10^{-3}^{\circ}\text{C/sec}$ to 10^6°C/sec , the data conform approximately to a straight line (on log-log scales) whose slope is about one-third.

For comparison with the structures of this alloy in the unidirectionally solidified plates, Figures 4-8 and 4-9 show the dendrite structure at slower and faster cooling rates. Figure 4-8 shows a furnace cooled sample (.44°C/sec cooling rate) and Figure 4-9 shows the structure of two splatted samples (at 2×10^5 and $2 \times 10^6^{\circ}\text{C/sec}$ cooling rates).

C. Discussion

The importance of "coarsening" or "ripening" in determining dendrite arm spacing has been the subject of a number of recent studies⁵⁻⁹ and these will not be reviewed here. In brief, these studies strongly suggest that final dendrite arm spacing over a very wide range of cooling rates is determined primarily by the rate of disappearance of dendrite arms during solidification, not by the number that initially form. Driving force for this disappearance of dendrite arms is reduction of liquid-solid surface energy.

Calculations on this ripening⁵ (based on a very simple model) indicate the critical time for disappearance of a dendrite arm, t_{crit} , is proportional to the following group of variables:

$$t_{crit} \propto \frac{HC_L(1 - k)md^3}{DT} \quad (4-1)$$

where H = volumetric heat of fusion

C_L = liquid composition

k = equilibrium partition ratio

m = liquid slope

d = dendrite arm spacing at time of interest

D = liquid diffusion coefficient

T = temperature

Insertion of reasonable values for iron-26% nickel alloy in equation (4-1) indicate ripening should occur in these alloys at least as fast as in other alloys for which it has previously been shown experimentally to occur. The linear dependency in Figure 4-7 of dendrite arm spacing on cooling rate is strong evidence that ripening controls the final spacing over this wide range of cooling rates.

Note that it should not be surprising that ripening can occur at the extremely short times involved in splat-cooling (or chill casting). Ripening is expected to be significant when:

$$\frac{t_{crit}}{t_f} \ll 1 \quad (4-2)$$

where t_f = local solidification time.

Experimental measurements⁵⁻¹⁵ have yielded, for a variety of alloys (including iron-26% nickel, Figure 4-7), the relation:

$$d_f^\nu = At_f = A'/\epsilon \quad (4-3)$$

where d_f = final dendrite arm spacing

ν, A, A' = constants

ϵ = cooling rate

Now, from (4-1) and (4-3), taking d as a constant fraction of d_f :

$$\frac{t_{\text{crit}}}{t_f} \propto d_f^{3-\nu} \quad (4-4)$$

Thus, when $\nu = 3$, t_{crit}/t_f is a constant regardless of cooling rate, and ripening can be expected to be equally important at very fast cooling rates as at very slow cooling rates. When $\nu < 3$, extent of ripening is expected to be more rapid at very fast cooling rates than at slower ones.

Most experiments on cast alloys have shown ν to be between 2 and 3, and in these cases, therefore, ripening effects should be at least as important as fast as at slow cooling rates. Note that in this work (Figure 4-7), ν is very nearly equal to 3.

Equation (4-1) is certainly an oversimplified picture of the ripening process, but qualitative conclusions to be gained from it, such as the above considerations of effect of cooling rate on importance of ripening, seem justified. Further, the general idea that final observed dendrite structures in alloys are

strongly influenced by curvature effects (i.e., solidification) serves to explain other aspects of dendrite structures. As example, the tendency of dendrite arms to fill in to form "plates" now seems clearly to result from this effect.

At high fraction solids, liquid-solid surface area can be reduced more efficiently by filling in spaces between rods to form plates than by disappearance of dendrite arms. We conclude that when plates form, this is the primary mechanism. It seems unlikely that heat flow alone could lead to these plates (as has been previously suggested) since they are often observed particular to the heat flow direction as well as parallel to it (e.g., Figures 4-5, 4-6).

D. Conclusions

(1) Alloy analysis in all the alloys studied had relatively little effect on secondary dendrite arm spacing. For example, secondary arm spacings 2 inches from the chill in unidirectionally solidified ingots were between 75 and 90 microns in all the alloys (including iron-nickel, iron-nickel-carbon, iron-phosphorous, iron-copper).

(2) In iron-26% nickel, dendrite arm spacing varies linearly (on log-log scales) with cooling rate over a range of from $10^{-3}^{\circ}\text{C/sec}$ to 10^6°C/sec cooling rate. Ripening kinetics control final dendrite arm spacing over this entire range.

(3) Driving force for formation of plate-like structures is, like "ripening", primarily reduction of liquid-solid surface energy.

References

1. R. V. Barone, H. D. Brody, M. C. Flemings, "Investigation of Solidification of High Strength Steel Castings", M.I.T., Interim Report, Contract No. DA-19-020-ORD-5443(X), Army Materials Research Agency, 30 September 1964.
2. R. V. Barone, "Solute Redistribution and Dendrite Morphology in Iron Base Alloys", Sc.D. Thesis, M.I.T., 1966.
3. "Investigation of Solidification of High Strength Steel Castings", M.I.T., Interim Report, Contract No. DA-19-020-ORD-5443, Army Materials Research Agency, 1962.
4. R. W. Strachan, "A Technique for Levitation Melting, Under-Cooling and Splat Cooling of Metals and Alloys", Ph.D. Thesis, M.I.T., Department of Metallurgy, 1967.
5. T. Z. Kattamis, M. C. Flemings, "Dendrite Structure and Grain Size of Undercooled Melts", Trans. Met. Soc. AIME, v. 236, 1966, pp. 1523-1532.
6. T. Z. Kattamis, J. M. Coughlin, M. C. Flemings, "Influence of Coarsening on Dendrite Arm Spacing of Aluminum-Copper Alloys", accepted for publication, Trans. Met. Soc. AIME.
7. T. Z. Kattamis, M. C. Flemings, "Solidification of Highly Undercooled Castings", accepted for publication, Trans. A.F.S., v. 75, 1967.
8. T. Z. Kattamis, U. T. Holmberg, M. C. Flemings, "Influence of Coarsening on Dendrite Arm Spacing and Grain Size of Magnesium-Zinc Alloy", to be published.
9. P. J. Ahearn, M. C. Flemings, "Solute Redistribution in a Tin-Bismuth Alloy", to be published.
10. A. B. Michael and M. B. Bever, "Solidification of Aluminum-Rich Aluminum-Copper Alloys", Trans. AIME, v. 200, 1954, p. 47.
11. M. D. Reed, "The Effect of the Time of Solidification on the Dendrite Arm Spacing", S.B. Thesis, M.I.T., Department of Metallurgy, 1960.
12. P. E. Brown and C. M. Adams, Jr., "Fusion-Zone Structures and Properties in Aluminum Alloys", Welding Journal Research Supplement, December, 1960.
13. R. E. Spear and G. R. Gardner, "Dendrite Cell Size", A.F.S. Transactions, v. 71, 1963, pp. 209-215.

14. J. A. Horwath and L. F. Mondolfo, "Dendritic Growth", *Acta Metallurgica*, v. 10, 1962, p. 1037.
15. H. Matyja, B. C. Giessen, N. J. Grant, "Effect of Cooling Rate on Dendrite Arm Spacing in Aluminum Alloys", to be published.

TABLE 4-1

Experimental Data on Cooling Rates and
Dendrite Arm Spacings, Iron-26 per cent
Nickel Alloy

Casting Type	Cooling Rate °C/sec	Secondary Dendrite Arm Spacing (microns)	Source
Furnace-cooled	4.62	65	This work ⁽³⁾
"	1.36×10^{-1}	77	" "
"	6.35×10^{-2}	145	" "
"	4.54×10^{-3}	280	" "
"	4.36×10^{-3}	280	" "
"	4.28×10^{-3}	280	" "
"	1.2×10^{-3}	605	" "
Unidirectional Plate			
1/2" from chill	9.6	40	This Work
1" " "	3.4	55	" "
2" " "	1.04	80	" "
4" " "	2.9×10^{-1}	120	" "
Splat	2.0×10^6	.55	Strachan ⁽⁴⁾
"	2.0×10^6	.60	"
"	1.0×10^6	.85	"
"	5.0×10^5	1.25	"
"	5.0×10^5	1.00	"
"	3.3×10^5	1.10	"
"	2.5×10^5	1.8	"
"	2.5×10^5	1.25	"
"	2.0×10^5	1.25	"
"	1.0×10^5	2.40	"
"	8.0×10^4	1.3	"
"	8.0×10^4	1.25	"

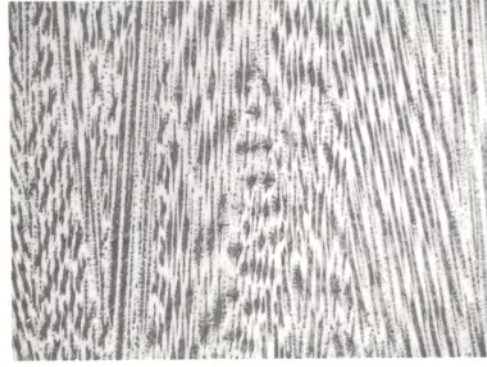
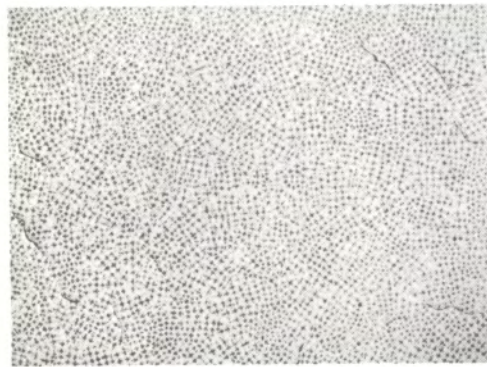
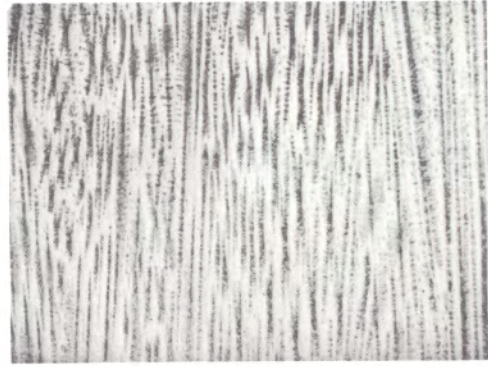
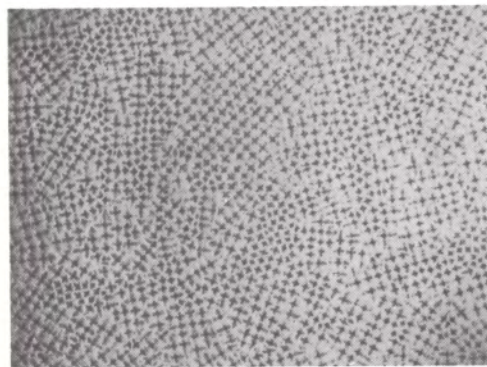


Figure 4-1. Iron-26 per cent nickel alloy. Photomicrographs at 1", 2", and 4" from the chill. 7.6X.

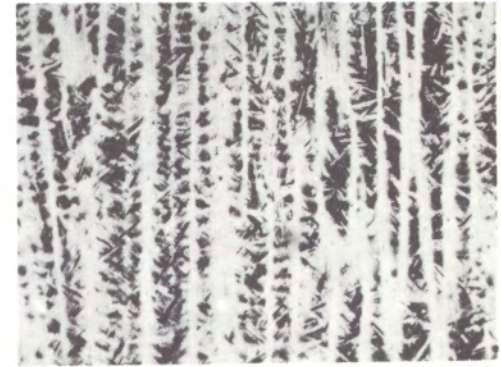
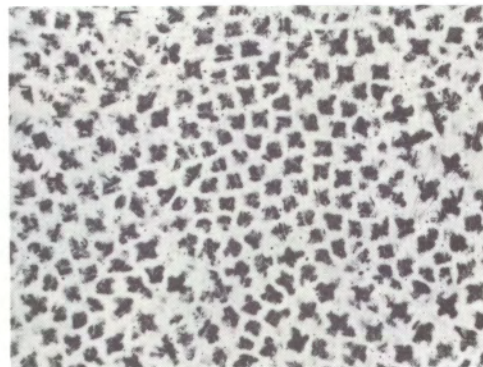


Figure 4-2. Iron-26 per cent nickel alloy. Photomicrographs at 1", 2", and 4" from the chill. 34X.

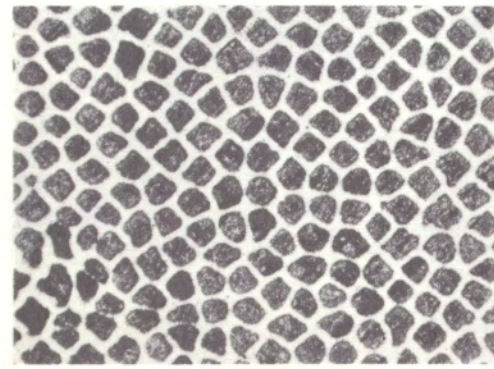
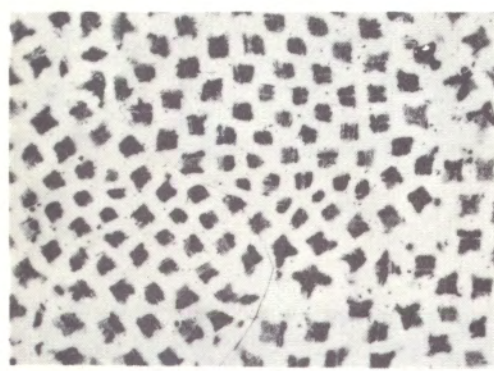
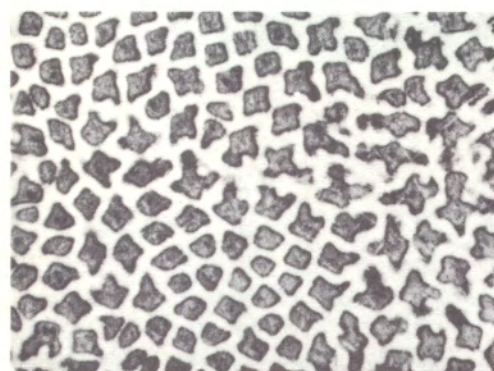
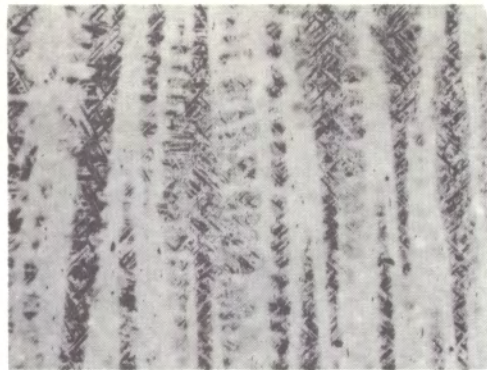
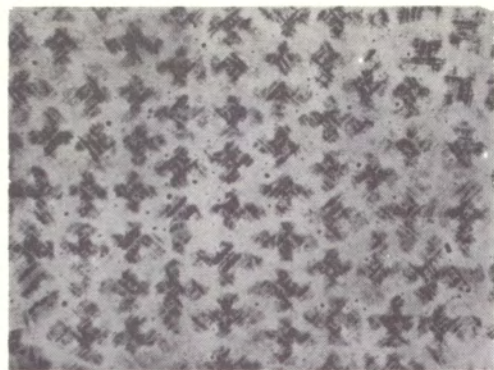


Figure 4-3. Iron-nickel alloys containing 10 per cent to 26 per cent nickel. Photomicrographs at 2" from the chill. 34X.

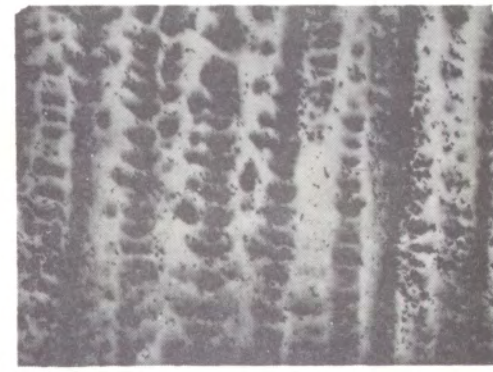
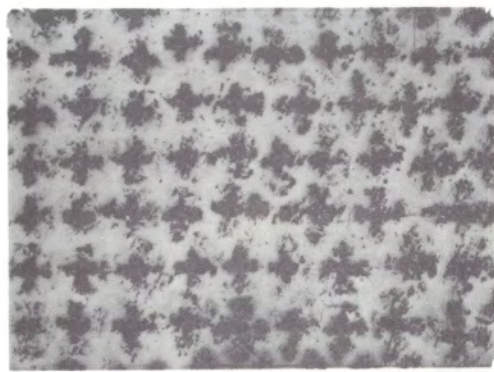
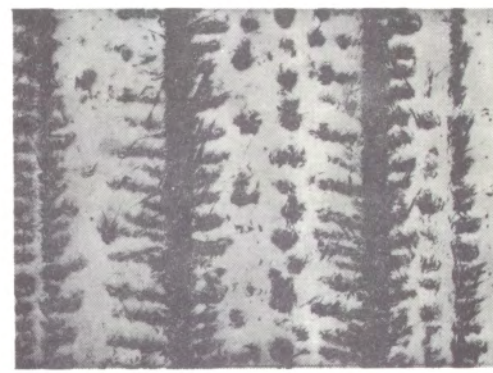
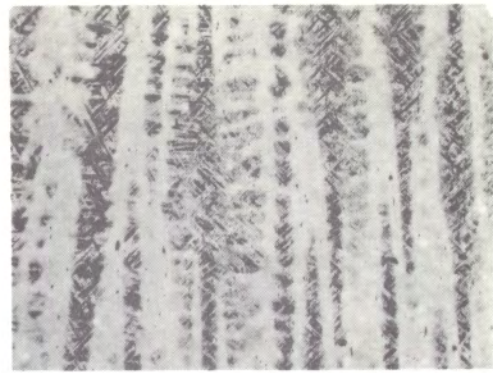
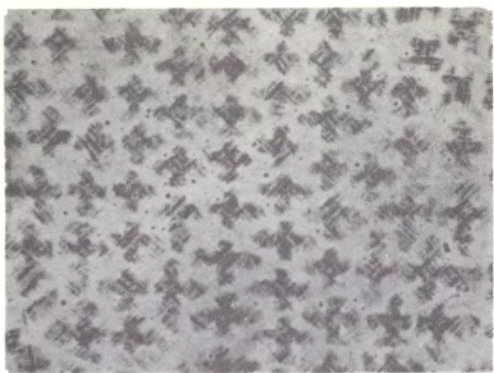


Figure 4-4. Iron-26 per cent nickel alloys containing 0 per cent carbon to 0.42 per cent carbon. Photomicrographs at 2" from the chill. 34X.

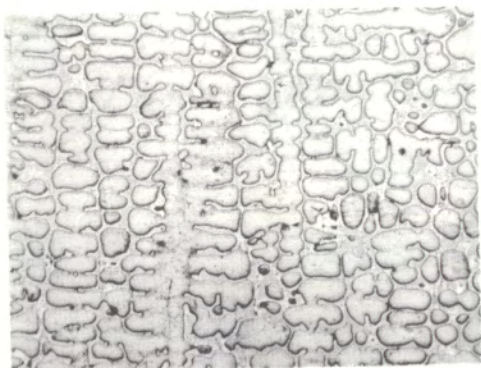
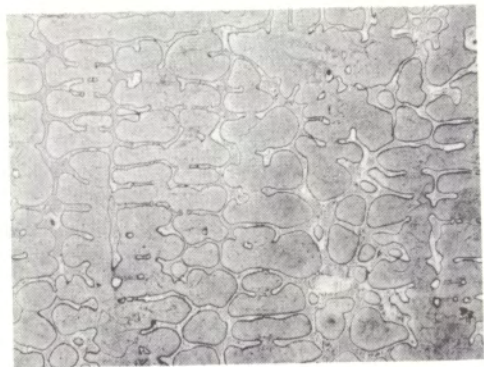


Figure 4-5. Iron-4 per cent phosphorous alloy. Photomicrographs at 1", 2", and 4" from chill. 34X.

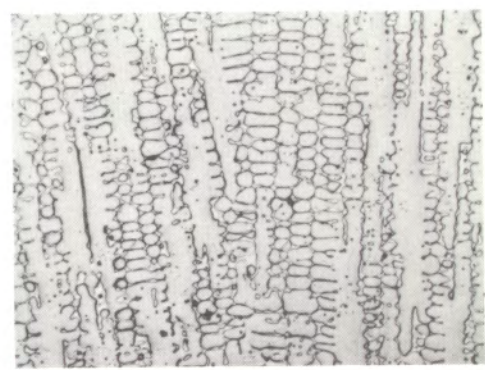
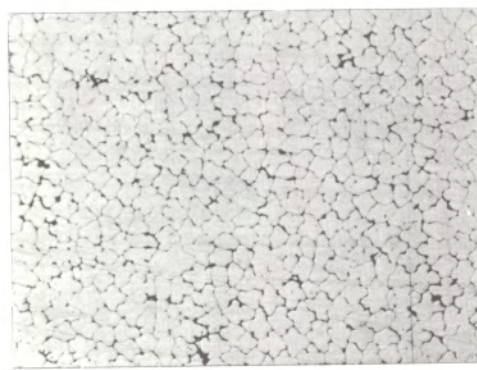
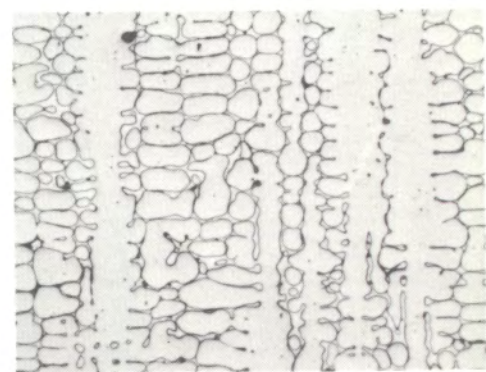
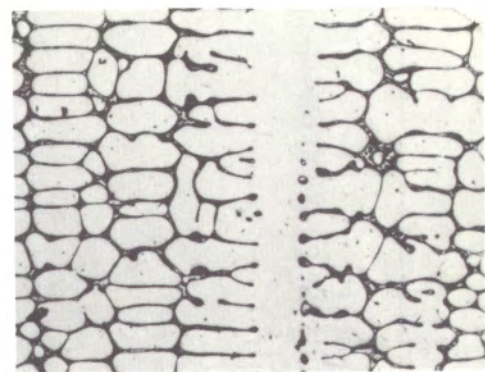


Figure 4-6. Iron-25 per cent copper alloy. Photomicrographs at 1", 2", and 4" from the chill. 64X.

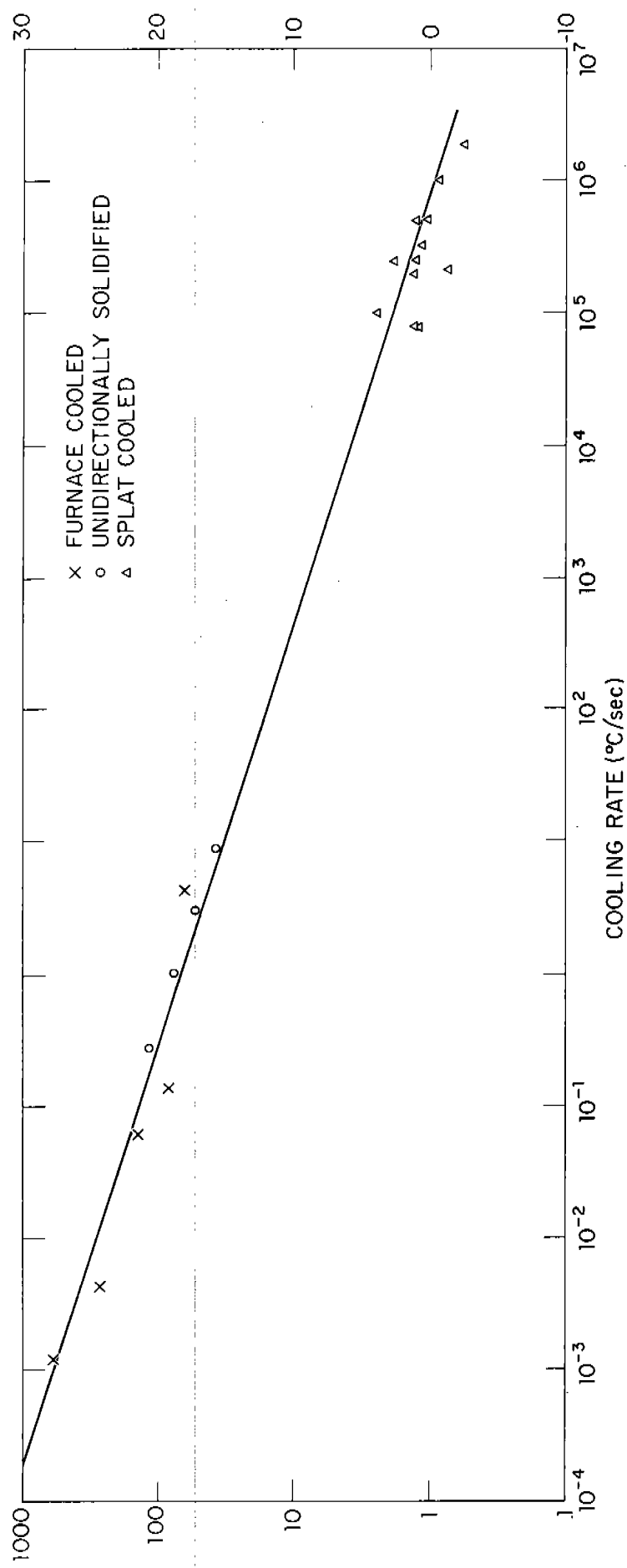


Figure 4-7. Dendrite arm spacing versus cooling rate, Fe-26 per cent Ni alloy. Furnace-cooled data from Mollard³, splat-cooled data from Strachan⁴.

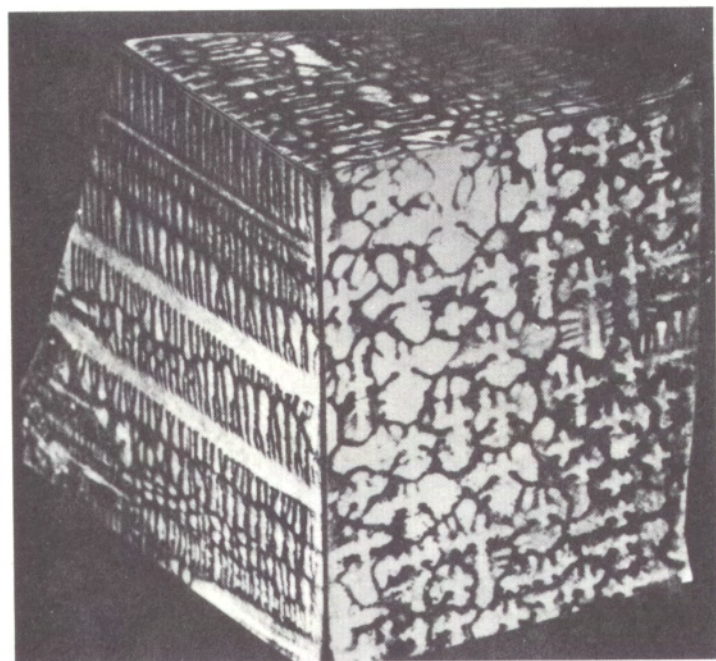


Figure 4-8. Three-dimensional view of iron-26 per cent nickel sample furnace cooled at $4.3 \times 10^{-3} \text{ }^{\circ}\text{C/sec}^3$.

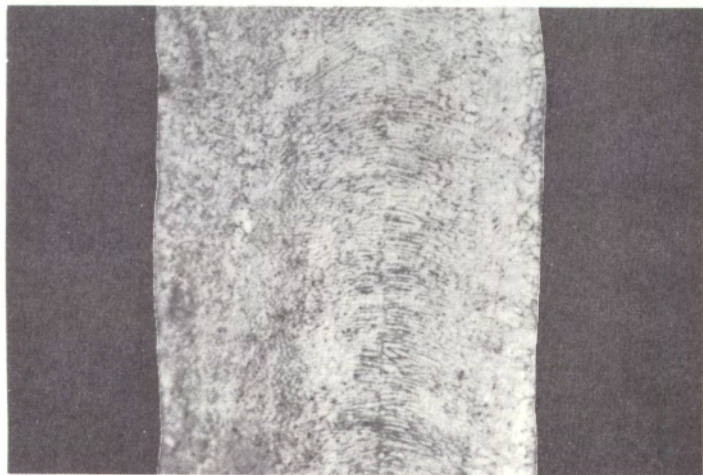
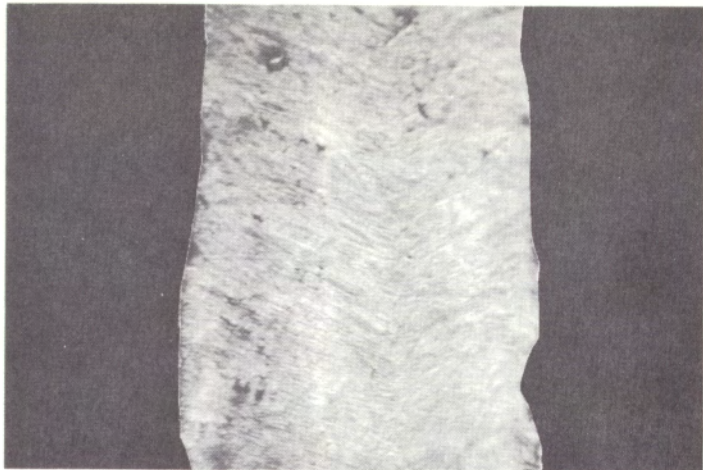


Figure 4-9. Two splat cooled samples, iron-26 per cent nickel alloy⁴.
Top- $2 \times 10^6^{\circ}\text{C/sec}$ cooling rate, 1000X.
Bottom- $2 \times 10^5^{\circ}\text{C/sec}$ cooling rate, 500X.

CHAPTER 5 - MICROSEGREGATION

A. Procedure

Chemical segregation existing in the iron-nickel and iron-phosphorous alloys was determined by electron microprobe analysis. Traces were made on samples taken in a plane transverse to the primary growth direction. Maximum and minimum solute contents were measured and "segregation ratios" calculated.

In addition, volume per cent eutectic in the iron-phosphorous system was measured by point counting in the following way. The polished and etched structure was projected on the ground glass screen of the metallograph at 60X. A grid of 63 points was placed over the field of view and the points that fell on the phase were counted. Between 30 and 60 grid positions were counted for each sample so that a total of 2000 to 4000 counts were amassed. The ratio of points falling in the eutectic was compared to total number of points yielded per volume fraction in the second phase. Error was estimated as described by Hilliard and Cahn¹ and is shown in Table 5-7.

B. Iron-nickel Binary Alloys

For comparison with later work, Tables 5-1 and 5-2 summarize some results on microsegregation in iron-26% nickel alloy obtained in a previous phase of this research and reported earlier². Small samples were cooled at controlled rate in an atmosphere furnace. Results showed the following:

1. Segregation ratio is not strongly affected by cooling rate (Table 5-1).
2. Significant diffusion occurs in the alloy during and after solidification. This was shown by rapid quenching of samples from at, and just below the solidus temperature (Table 5-2). Even samples quenched from just at or above the solidus showed much less segregation than would be predicted by the "non-equilibrium lever rule".

Table 5-3 summarizes results of detailed microprobe studies on unidirectionally solidified iron-26% nickel and iron-10% nickel alloys, a portion of which have been presented earlier³. Segregation ratio decreases slightly with increasing distance from the chill in iron-26% nickel, but not at all in iron-10% nickel. Solidification times at these various locations were determined as described in Chapter 3, and dendrite arm spacings measured from photomicrographs such as those in Chapter 4. Results are listed in Table 5-4.

Experimental and calculated segregation ratios are compared in Table 5-5 for these two alloys. The "calculated" ratios were obtained in the following way:

- (1) Values of η were calculated from data of Table 5-4, where

$$\eta = \frac{4t_f}{(gd)^2}$$

t_f = solidification time

d = dendrite arm spacing (primary or secondary)

g = correction factor (as given in footnotes of Table 5-4)

(2) Calculated segregation ratio at room temperature, S_C° , were then determined directly from the appropriate figure of Chapter 2.

The correction factors, g , applied to the dendrite arm spacing were arbitrary except that the same correction factor was used for both alloys and all solidification times. The factor chosen was that which, for a given model, gave closest agreement with experiment. These were:

Plate model, primary spacing $g = 0.13$

Plate model, secondary spacing $g = 0.30$

Cylinder model, primary spacing $g = 0.17$

Cylinder model, secondary spacing $g = 0.40$

A correction factor, g , of 1 would indicate direct correspondence of experiment with theory. Factors less than 1 indicate considerably less segregation than that predicted. Note that the cylindrical models give closer correspondence with experiment, but the required correction factor is still significantly less than 1.0. This is discussed further below.

C. Iron-nickel-carbon Alloys

Carbon was added to an iron-26% nickel alloy in amounts up to 0.42%, and segregation ratios measured, Table 5-6. No

significant effect was measured. A result considerably different from that is obtained when carbon is added to iron-chromium alloy⁴.

D. Iron-4% Phosphorous Alloy

Results of lineal analysis of the iron-4% phosphorous alloy are listed in Table 5-7. The per cent eutectic decreases only slightly with increasing distance from the chill. Moreover, using solidification times and dendrite arm spacings listed in Table 5-8, results agree with experiment assuming correction factors, g , are not greatly different than those for the iron-nickel alloys ($g = 0.19$ for primary spacing, plate model; $g = .56$ for secondary spacing, plate model). Results are listed in Table 5-9.

Table 5-10 lists minimum solute contents measured with the microprobe. In agreement with experiments on other alloys, these minima are also relatively constant with increasing distance from the chill. However, they are substantially higher than would be predicted from Figure 2-11 using correction factors, g , such as have been used above. Much smaller factors ($g < 0.10$) must be employed. The reason for the higher solute content than expected (and hence lower required g) is not known.

E. Discussion

When early work was conducted on microsegregation in ferrous and non-ferrous alloys, it was observed that correction factors of about 0.2 to 0.3 (applied to dendrite arm spacing) were

necessary to make experiment and theory correspond. At that time, only a single plate model was employed, and the procedure employed was valid only for relatively small amounts of diffusion in the solid during and after solidification.

Work reported in Chapter 2 of this report was therefore undertaken to permit better correspondence of theory with experiment. A computer analysis valid for extensive diffusion was developed. Also, a cylindrical dendrite model, as well as plate-like dendrite model, was examined. Agreement with experiment, as noted above, was better. For iron-nickel alloys, the correction factor rose as high as 0.4 (for cylindrical model, secondary spacing) but this factor is still too far from 1 to be explained by considerations such as inaccurate diffusion data, more complex dendrite geometry, etc.

The discrepancy is resolved only in the light of recent experiments, mentioned previously in Chapter 4, which show that substantial "ripening" or "coarsening" occurs during dendritic solidification⁵⁻⁹. In essence, the neglect of curvature effects is now shown to be an imperfect approximation. In fact, the curvature effects mean that throughout dendritic solidification, small arms are disappearing, and larger ones growing at their expense. The dendrite arm spacing finally observed in a casting or ingot is not that existing throughout freezing but is much coarser than that that was present relatively early in freezing.

Thus, the correction factor, g , reflects in part at least, the fact that average dendrite arm spacing during solidification is significantly smaller than that finally observed. Considerable solid diffusion, previously unaccounted for, is taking place in small dendrite arms which are "remelting" and re-precipitating on the larger arms throughout solidification.

F. Conclusions

1. Segregation ratio in iron-26% nickel alloy decreases only slightly with increasing distance from the chill. Segregation ratio in iron-10% nickel alloy is essentially constant.
2. In iron-4% phosphorous alloys, amount of second phase and minimum solute content are essentially constant with increasing distance from the chill.
3. Carbon in amounts up to 0.42% does not significantly affect segregation ratio of iron-26% nickel alloy.
4. Good agreement of calculated segregation with that experimentally observed in iron-nickel alloys is obtained, provided calculations are based on measured dendrite arm spacing times a correction factor, g . The required correction factor depends on dendrite model employed but not on solidification time or alloy content. Depending on the model employed, g lies between 0.17 and 0.40.

5. It appears that the need for a correction factor, g , arises primarily because of the "coarsening" or "ripening" now known to occur during dendritic solidification.

6. In agreement with theory, segregation ratio of iron-10% nickel alloy is greater than that in iron-26% nickel alloy.

References

1. T. E. Hilliard and J. W. Cahn, "An Evaluation of Procedures in Quantitative Metallography for Volume Fraction Analysis",
2. "Investigation of Solidification of High Strength Steel Castings", M.I.T., Interim Report, Contract No. DA-19-020-ORD-5443, Army Materials Research Agency, 1962.
3. R. V. Barone, H. D. Brody, M. C. Flemings, "Investigation of Solidification of High Strength Steel Castings", M.I.T., Interim Report, Contract No. DA-19-020-ORD-5443(X), Army Materials Research Agency, 30 September 1964.
4. D. Poirier, M. C. Flemings, "Investigation of Solidification of High Strength Steel Castings", M.I.T., Interim Report, Contract No. DA-19-020-ORD-5443(X), October, 1963.
5. T. Z. Kattamis, M. C. Flemings, "Dendrite Structure and Grain Size of Undercooled Melts", Trans. Met. Soc., AIME, v. 236, 1966, pp. 1523-1532.
6. T. Z. Kattamis, J. M. Coughlin, M. C. Flemings, "Influence of Coarsening on Dendrite Arm Spacing of Aluminum-Copper Alloys", accepted for publication, Trans. Met. Soc., AIME.
7. T. Z. Kattamis, M. C. Flemings, "Solidification of Highly Undercooled Castings", accepted for publication, Trans. A.F.S., v. 75, 1967.
8. T. Z. Kattamis, U. T. Holmberg, M. C. Flemings, "Influence of Coarsening on Dendrite Arm Spacing and Grain Size of Magnesium-Zinc Alloy", to be published.
9. P. J. Ahearn, M. C. Flemings, "Solute Redistribution in a Tin-Bismuth Alloy", to be published.

Table 5-1
Furnace Cooled Iron-25% Nickel Alloy*

Cooling Rate (°C/sec)	Dendrite Arm Spacing (d)	C_M	C_m	S°
.14	77	28.2	22.8	1.23
6.4×10^{-2}	145	28.7	22.8	1.25
4.3×10^{-3}	280	30.7	26.7	1.15

* Samples were water-quenched 55°C below the liquidus temperature.

Table 5-2

Segregation Ratio in Interrupted Cooling Experiments(Cooling Rate 4.3×10^{-3} °C/sec)

<u>Quenching Temperature</u>	<u>C_M</u>	<u>C_m</u>	<u>C_M/C_m</u>
$T_M = 21^\circ\text{C}$	30.2	23.5	1.29
$T_M = 25^\circ\text{C}$	29.7	25.5	1.17
$T_M = 55^\circ\text{C}$	30.7	26.7	1.15

Note: Non-equilibrium solidus is approximately $T_M = 25^\circ\text{C}$
 (see footnote to equation 3-2).

Table 5-3
Electron Probe Microanalyzer Results

Alloy	Distance from chill (inches)	C_M° (% Ni)	C_m° (% Ni)	S_e° C_M°/C_m°
Fe-26% Ni				
	1/2	32.6	25.5	1.28
	1	30.0	24.5	1.26
	2	29.5	25.2	1.17
	4	29.8	25.2	1.18
Fe-10% Ni				
	1/2	11.6	8.59	1.35
	1	11.3	8.58	1.32
	2	11.6	8.40	1.38
	4	11.6	8.40	1.38

Table 5-4

Measured Dendrite Arm Spacing and Solidification Times
in Iron-Nickel Alloys

Alloy	Distance from chill (inches)	Primary dendrite arm spacing, d_p (microns)	Secondary dendrite arm spacing, d_s (microns)	Solidification time, t_f (seconds)
Fe-26% Ni	1/2	70	40	2.6
Fe-26% Ni	1	100	55	7.5
Fe-26% Ni	2	190	80	24
Fe-26% Ni	4	360	120	86
Fe-10% Ni	1/2	50	-	2.6
Fe-10% Ni	1	75	-	7.5
Fe-10% Ni	2	125	80	24
Fe-10% Ni	4	235	150	86

Table 5-5

Comparison of Measured and Calculated Segregation
Ratios in Iron-Nickel Alloys

Alloy	Location (inches from chill)	Measured Segregation Ratio, S_e^o	Exp.	Calculated Segregation Ratios, S_c^o			(4)
			(1)	(2)	(3)		
Fe-26% Ni	1/2	1.28	1.29	1.42	1.29	1.32	
Fe-26% Ni	1	1.22	1.22	1.21	1.21	1.29	
Fe-26% Ni	2	1.17	1.17	1.23	1.23	1.22	
Fe-26% Ni	4	1.18	1.18	1.23	1.23	1.12	
Fe-10% Ni	1/2	1.35	1.35	-	1.58	-	
Fe-10% Ni	1	1.32	1.32	-	1.35	-	
Fe-10% Ni	2	1.38	1.38	-	1.33	-	
Fe-10% Ni	4	1.38	1.38	-	1.33	-	

(1) Based on plate model, using primary dendrite arm spacing times 0.13 to calculate η .

(2) Based on plate model, using secondary dendrite arm spacing times 0.30 to calculate η .

(3) Based on cylinder model, using primary dendrite arm spacing times 0.17 to calculate η .

(4) Based on cylinder model, using secondary arm spacing times 0.4 to calculate η .

Table 5-6

The Effect of Carbon on Microsegregation
in an Iron-26% Nickel Alloy - 2 Inches
from the Chill

Chemical Analysis	C_M°	C_m°	S_e°
	Wt. % C	Wt. % Ni	Wt. % Ni
0	29.5	25.5	1.17
.33	26.8	22.4	1.19
.42	26.4	22.7	1.16

Table 5-7

Volume Per Cent Eutectic Measured Metallographically
at Different Distances from the Chill

Distance from the Chill	Volume Per Cent	Weight Per Cent
1"	28.3 \pm 1.5*	26.4
2"	28.5 \pm 1.5*	26.5
3"	27.5 \pm 1.5*	25.7
4"	27.0 \pm 1.5*	25.2

Table 5-8

Measured Dendrite Arm Spacings and Solidification Time
in Iron-4% Phosphorous Alloy

Distance from chill (inches)	Primary dendrite* arm spacing, d_p , (microns)	Secondary dendrite arm spacing, d_s , (microns)	Solidification time, t_f (seconds)
1	122	50	7.5
2	220	73	24
3	300	100	51
4	380	108	86

Table 5-9

Comparison of Measured and Calculated Weight Per Cent Eutectic in Iron-4.0 Per Cent Phosphorous Alloy

Location (inches from drill)	Experimentally Measured Weight Per Cent Eutectic	Calculated Weight Per Cent Eutectic	(2)
(1)	26.4	26.3	26.8
2	26.5	26.2	26.1
3	25.7	26.0	25.8
4	25.2	25.7	25.0

(1) Based on plate model, using primary dendrite arm spacing times 0.19 to calculate n .

(2) Based on plate model using primary dendrite arm spacing times 0.56 to calculate n .

Table 5-10

Electron Microprobe Analysis for Minimum Phosphorus
Contents at Different Distances from the Chill

Distance from the chill X, (inches)	Minimum Solute Content C_m (wt. % P)
1/2	2.2
2	2.1
4	2.0

APPENDIX A: List of Symbols

C_L	Composition of the liquid within the volume element
C_M^*, C_M^o	Local maximum solid composition at non-equilibrium solidus and at room temperature, respectively
C_m^*, C_m^o	Local minimum solid composition at non-equilibrium solidus and at room temperature, respectively
C_s	Solid composition within the dendrite
$C_{s,j,k}$	Solid composition in the j slice and at the k interval of time
C_s^*	Solid composition at the liquid solid interface
d	Dendrite arm spacing at time of interest
d_f	Final dendrite arm spacing
D, D_s	Diffusion coefficient in liquid and solid phases, respectively
f_E, f_L, f_s	Weight fraction eutectic, liquid, solid, respectively
g	Microsegregation correction factor
H	Volumetric heat of fusion
k	Partition ratio
L	One half the dendrite arm spacing
M	$\Delta\lambda^2/D_s \Delta t$
m	Slope of the liquidus
s^*, s^o	Segregation ratio, C_M/C_m , at the non-equilibrium solidus and at room temperature, respectively
t	Time from the beginning of solidification within the volume element
t_f	Local solidification time
t'	Time from beginning of solidification of the ingot
t_{crit}	Critical time for disappearance of a dendrite arm

T	Absolute temperature
X	Distance from the chill
x_L, x_S	Position of liquidus and solidus, respectively
α	$D_s t_f / L^2$
ε	Cooling rate
λ	Distance from the dendrite centerline
λ_i	Position of the solid liquid interface within the volume element
η	t_f / L^2

APPENDIX B: Method III - Finite Difference.
Mass Balance Technique

The major assumptions of the solidification model are presented at the beginning of Chapter 2. First consider the dendrites to be plate-like and the characteristic volume element to be as in Figure B-1. The initial condition for the computation is

$$\text{when } t = 0, \lambda_i = 0, C_s(\lambda_i) = kC_o, C_L = C_o \quad (B-1)$$

The mechanics of the numerical technique are illustrated in Figure B-1 and are described below.

The Solidification Interval

(1) The composition distribution in the solid of a plate-like dendrite is schematically represented by the heavy line ($C_{s_{j,k}}$) in Figure B-1 where the subscript j indexes the position of the slice and the subscript k refers to intervals of time. The composition of the liquid is calculated from the mass balance

$$C_{L_k} = \frac{C_o - \frac{1}{L} \sum_{j=1}^{j^*} C_{s_{j,k}} \Delta \lambda}{\lambda_i} \quad (B-2)$$

where

$$f_s = \frac{\lambda_i}{L} \quad (B-3)$$

and j^* refers to the slice at the liquid solid interface. (Note: For the first step $C_L = C_o$)

(2) The interface is advanced a distance $\Delta\lambda$ by transformation of an increment of solid of composition $C_{s_{k+1}}(\lambda)$ which is in equilibrium with the liquid C_{L_k} as given by the phase diagram.

(3) The temperature of the volume element is determined from the phase diagram and the value of C_{L_k} .

(4) Diffusion is allowed to occur in the solid for an amount of time Δt which is the time elapsed as the interface moves ahead one slice from λ_{i_k} to $\lambda_{i_{k+1}}$.

Solid diffusion is computed by iteratively evaluating the finite difference algorithm for Fick's Second Law

$$C_{s_{j,k}} = \frac{C_{s_{j+1,k-1}} + (M - 2) C_{s_{j,k-1}} + C_{s_{j-1,k-1}}}{M} \quad \dots \quad (B-4)$$

where

$$M = -\frac{\Delta\lambda^2}{D\Delta t} \quad \dots \quad (B-5)$$

for each slice within the solid, $1 \leq j \leq j^*$. The elapsed time, t , may be computed from the linear or parabolic growth expressions (equations 2-1 or 2-2) or from thermal data, in the form of an expression or table, that relates temperature and time. If the diffusion coefficient, D_s , is a function of both

* H. S. Carslon, and J. C. Jaeger: Conduction of Heat in Solids, Clarendon Press, Oxford, 1959, p. 466.

temperature and composition, it must be re-evaluated for every iteration of the algorithm.

The finite difference approximation is most accurate for large values of M and the solution will be unstable for values of M less than two.* For this reason whenever $\Delta\lambda^2/D_s \Delta t$ was less than 4, diffusion was considered to take place over $p \geq 4 \Delta\lambda^2/D_s \Delta t$ time increments each $\Delta\theta$ in length, such that $\Delta\lambda^2/D_s \Delta\theta \geq 4$ and $p\Delta\theta = t$. The solution for the incremental time period Δt is then attained by repeating equation C-4 over all slices, j , p times.

The boundary conditions for this computation are

$$\text{at } \lambda = 0, \frac{\partial C_s}{\partial \lambda} = 0; \text{ and at } \lambda = \lambda_i, C_s = C_{s_k}(\lambda_i) \quad (B-6)$$

where $C_{s_k}(\lambda_i)$ is computed by mass balances as in steps (1) and (2). And the composition of the first slice in the $-\lambda$ direction is always set equal to the composition computed for the first slice in the $+\lambda$ direction. Thus, the flux across $\lambda = 0$ is zero.

(5) After diffusion has occurred for a time Δt and a new composition distribution has been computed steps (1) through (4) are repeated; a new liquid composition is computed, the composition of a new solid increment and the temperature are found from the phase diagram and diffusion is again allowed to occur. The

* H. S. Carslon, and J. C. Jaeger: Conduction of Heat in Solids, Clarendon Press, Oxford, 1959, p. 466.

above procedure is repeated until the alloy is all solid or until a eutectic composition is reached in the liquid.

(6a) **Eutectic Systems:** During solidification of an alloy in a eutectic system, if the liquid composition reaches the eutectic composition at a time t_E , diffusion is computed in the primary phase at the eutectic temperature until solidification is completed, i.e., $\Delta t = t_f - t_E$. As a result of diffusion of solute into the primary phase, some eutectic must disappear; and this shift in the primary phase-eutectic interface is monitored throughout the calculation. The following boundary conditions are used in the computation from time t_E to t_f :

$$\lambda = 0, \frac{\partial C}{\partial \lambda} = 0; \lambda = \lambda_E, C_s^* = C_s \text{ (maximum solubility)} \quad (B-7)$$

where λ_E represents the distance to the eutectic interface.

In the special case that the last increment of solidification is reached (i.e., $\lambda_i = L - \Delta \lambda$) and the liquid composition is less than the eutectic composition and greater than the maximum solubility limit some eutectic is considered to have formed and the amount is given by

$$f_E = \frac{C_L - C_s \text{ (maximum solubility)}}{C_E - C_s \text{ (maximum solubility)}} \left(\frac{\Delta \lambda}{L} \right) \dots \quad (B-7)$$

where f_E = weight fraction eutectic

C_E = composition of the eutectic at the eutectic temperature

C_s (maximum solubility) = composition of the primary phase at the eutectic temperature

In the above two cases the non-equilibrium solidus temperature is considered to be the eutectic temperature.

In the case that the last increment of solidification is reached and the liquid composition is less than the maximum solubility limit, the computation is handled in the same manner as a single phase alloy.

(6b) Single Phase Alloy: Since the compositions gradients near the end of solidification are usually steep, the average composition of the last increment to freeze may not be a good indication of the non-equilibrium solidus temperature. It is often desirable to look at the last slice to freeze in more detail (and in the time sharing version of this program the decision is left to the human operator, see Appendix D). When desirable, the last increment to freeze is divided into smaller slices and the composition distribution within that increment calculated in greater detail. The last increment is broken into one fifth the number of slices that were used in the original computation and the analysis repeated for the new C_o , L , and θ_f . The factor of 0.2 was found to be adequate to describe the final solidification and the keep computer time reasonable. The composition of the last solid to freeze in this

final calculation is then used to define the non-equilibrium solidus temperature.

Cooling from the Non-Equilibrium Solidus

Following the completion of solidification, the change in solute redistribution that occurs on cooling from the non-equilibrium solidus to room temperature may be computed using the finite difference technique. The cooling rate relation may be input to the computer from hypothetical or empirical tabular data or in the form of an expression. The cooling rate relation defines the time for diffusion within each temperature interval and the diffusion coefficient is calculated on the basis of the average temperature within the temperature interval. The amount of diffusion is computed by evaluation of the algorithm (B-4) at each slice j within each temperature interval and the size of the temperature interval is chosen to keep M greater than 4. The initial condition is the solute distribution at the solidus temperature. The boundary conditions for a single phase alloy are

$$\lambda = 0, \frac{\partial C}{\partial \lambda} = 0; \quad \lambda = L, \frac{\partial C}{\partial \lambda} = 0 \quad (B-9)$$

and for a eutectic alloy

$$\lambda = 0, \frac{\partial C}{\partial \lambda} = 0; \quad \lambda = L(1 - f_E), \quad C_S^* = C_S \text{ (max. solubility)} \quad \dots \quad (B-10)$$

Computations are continued until room temperature is reached or until the effect of diffusion on microsegregation becomes negligible.

Cooling Curves: Since diffusion can be described in terms of η values it is convenient to choose a one second solidification time and to vary the dendrite arm spacing in order to get the microsegregation parameters in terms of η . If actual cooling curves are to be used, this procedure necessitates the readjustment of the data to produce a meaningful result.

Iron-Nickel: To evaluate the cooling rates for various value of η , the six thermocouple measurements taken at various distances from the chill in an iron-26% nickel alloy and described in Chapter 3 were plotted in a special way. First, the solidification range was taken to be 25°C . The time to drop 25°C was measured from each cooling curve and the six values defined as the solidification times, t_f . Temperature readings were then taken from each curve at multiples of its own t_f and plotted. The resulting curves overlapped and deviated less than $\pm 15^{\circ}\text{C}$ down to 1150°C and approximately 18°C down to 1000°C . Three positions overlapped $\pm 10^{\circ}\text{C}$ all the way down to 1000°C . This allowed the master curve of temperature versus θ_f to be made which ranges from 1469.5 to 1000°C and is shown in Figure B-2. These values were then used for all η 's in the iron-nickel system as follows:

(1) The temperature of the zero time point of the master curve and the liquidus point for the alloy were made to coincide by shifting the master curve.

(2) The solidification temperature range for a given η is taken from the computer solution after solidification has occurred and a solidification time is obtained from the liquidus and solidus temperature, and the cooling curve. The solidification time is then compared with the assigned value, i.e., 1 second and the remaining times in the solidification curve adjusted by this factor.

Iron-Phosphorus: In the iron-phosphorus system cooling rates of 200°C/sec and 800°C/sec were used in conjunction with a 1 second solidification time.

Cylindrical Geometry: In some cases a cylindrical volume element may be of more interest than a plate-like volume element. In such a case the axis of the cylinder is considered to coincide with the dendrite spine and the liquid solid interface advances from the axis at time $t = 0$ to a radius of L at time t_f , where L is one half the dendrite arm spacing and t_f is the solidification time. The rate of advance of the interface may be given by a linear volume growth rate or a parabolic volume growth rate:

$$\frac{dV}{dt} = \text{constant: } r_i = \text{constant } \sqrt{t} \quad (B-11)$$

$$\frac{dV}{dt} = \frac{\text{constant}}{\sqrt{t}}: \quad r_i = \text{constant } 4\sqrt{t} \quad (B-12)$$

where r_i denotes the position along the radius of the solid-liquid interface. In addition, as with the plate-like model, the position of the interface may be calculated from a cooling curve. In cylindrical coordinates Fick's Second Law is written

$$\frac{\partial C}{\partial t} = D \left(\frac{\partial^2 C}{\partial r^2} + \frac{1}{r} \frac{\partial C}{\partial r} \right) \quad (B-13)$$

which is transformed by the finite difference method

$$C_{j,k} = \frac{(1 + \frac{0.5}{j-1}) C_{j+1} + (M - 2) C_j + (1 - \frac{0.5}{j-1}) C_{j-1}}{M} \quad \dots \quad (B-14)$$

The mechanics of the solution are the same as that used for the plate-like model except, now, equal slices are taken along the radius, the algorithm (B-14) is used to evaluate the diffusion in the solid and the rate of advance of the interface is given by expressions such as (B-11) or (B-12).

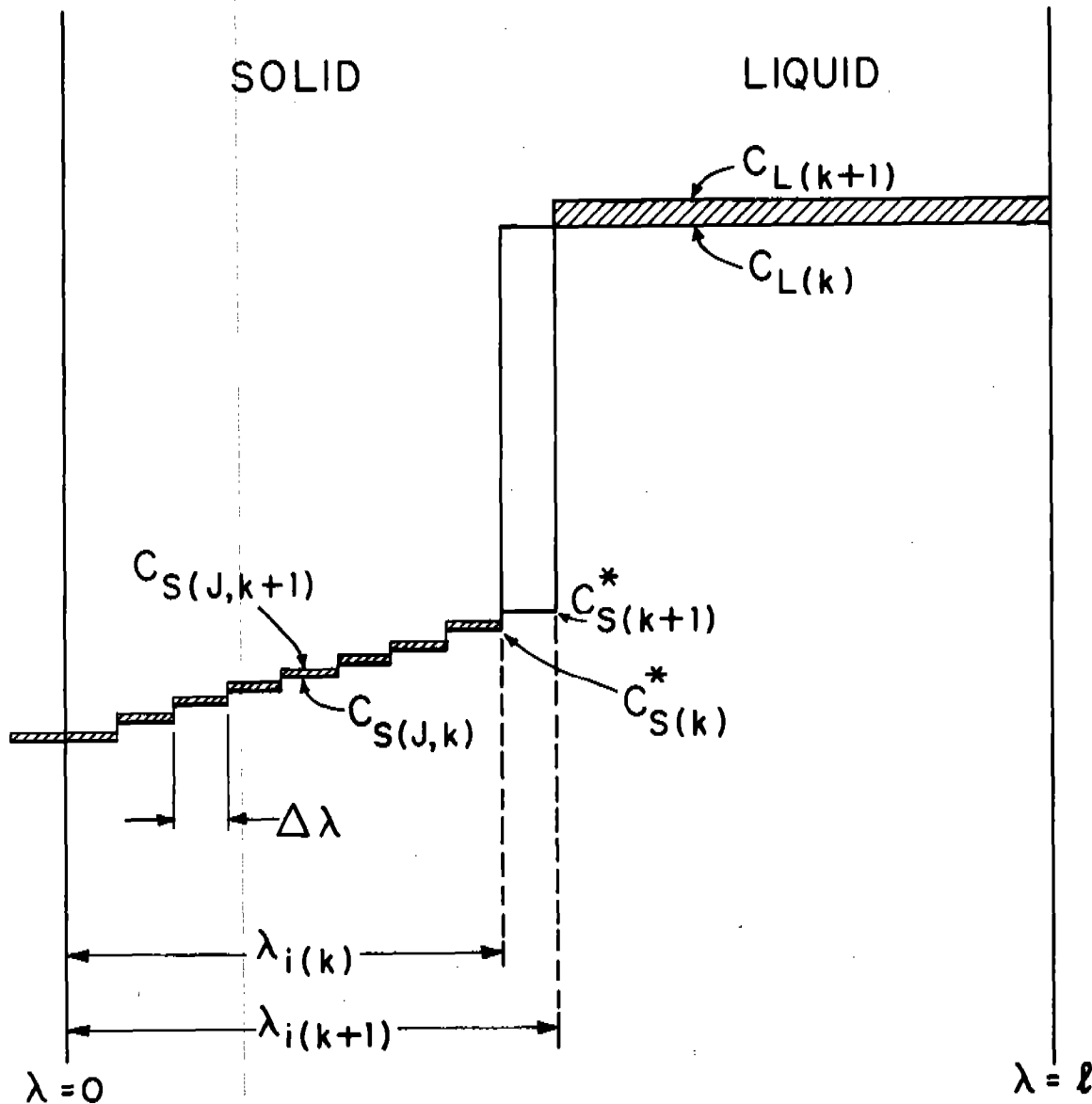


Figure B-1. Schematic diagram of the sequence of steps in the Mass Balance Technique for calculating solute redistribution in an alloy solidifying into a single solid phase of variable composition.

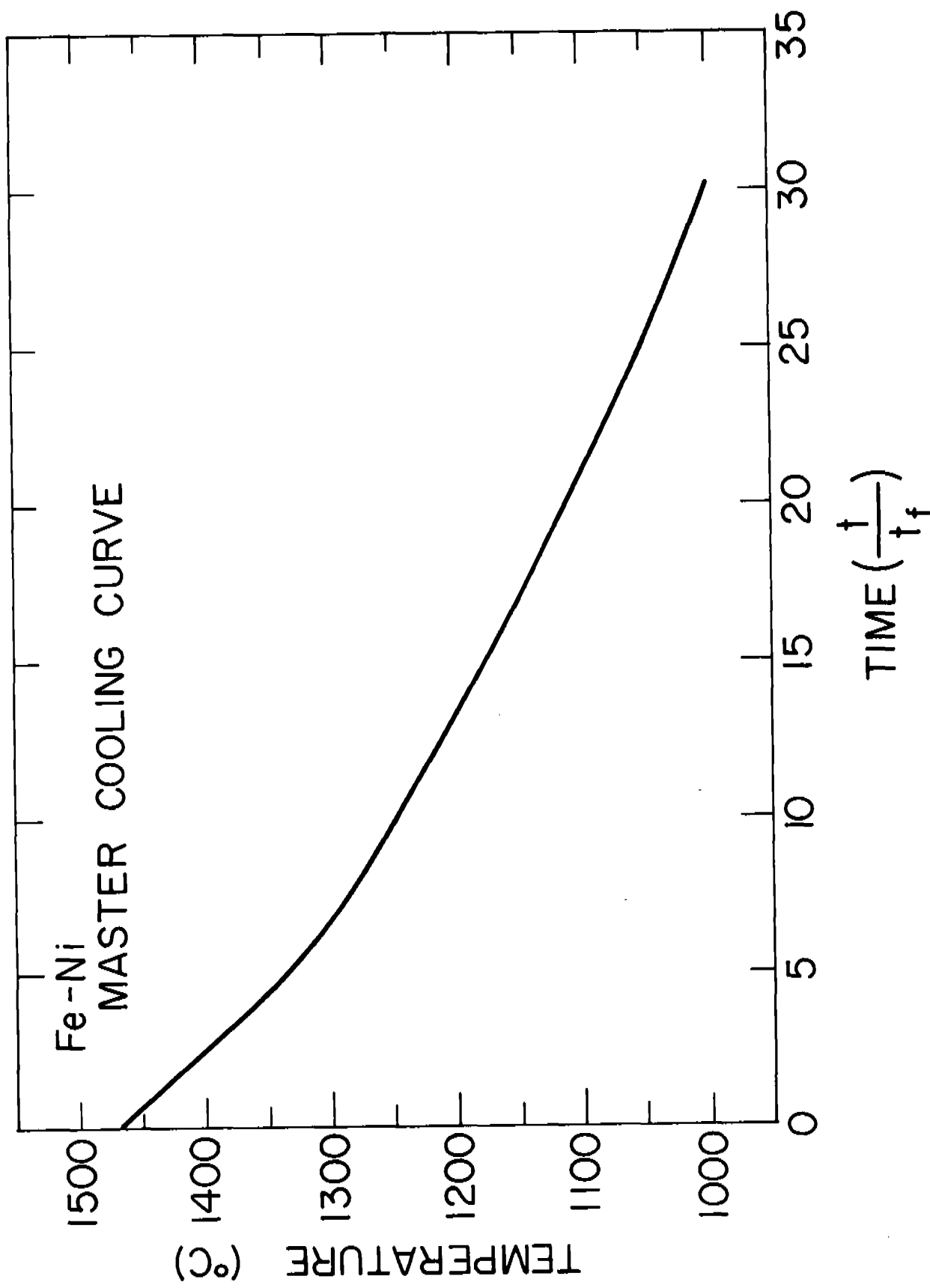


Figure B-2. Master cooling curve for iron-nickel alloys.

DISTRIBUTION LIST

	<u>No. of Copies</u>
Office of the Director Defense Research and Engineering The Pentagon Washington, D. C. 20301 Attn: Mr. J. C. Barrett Dr. Donald MacArthur	1 1
Commander Defense Documentation Center Cameron Station, Bldg. 5 5010 Duke Station Alexandria, Virginia 22314	20
Defense Metals Information Center Battelle Memorial Institute Columbus, Ohio 43201	2
National Aeronautics and Space Administration Washington, D. C. 20546 Attn: Mr. B. G. Achhammer Mr. G. C. Deutsch Mr. R. V. Rhode	1 1 1
National Aeronautics and Space Administration Marshall Space Flight Center Huntsville, Alabama 35812 Attn: R-P&VE-M, Dr. W. Lucas M-F&AE-M, Mr. W. A. Wilson, Bldg. 4720	1 1
U. S. Atomic Energy Commission Office of Technical Information Extension P. O. Box 62 Oak Ridge, Tennessee 37830	1
Chief of Research and Development Department of the Army Washington, D. C. 20310 Attn: Physical and Engineering Science Division	2
Headquarters Aeronautical Systems Division Wright-Patterson Air Force Base Wright-Patterson Air Force Base, Ohio 45433 Attn: ASRCEE	5

DISTRIBUTION LIST

No. of Copies

Chief
Office of Naval Research
Department of the Navy
Washington, D. C. 20360
Attn: Code 423 1

Commander
U. S. Naval Research Laboratory
Anacostia Station
Washington, D. C. 20390
Attn: Technical Information Officer 1

Commanding General
Deseret Test Center
Fort Douglas, Utah 84113
Attn: Technical Information Office 1

Commanding General
U. S. Army Electronics Command
Fort Monmouth, New Jersey 07703
Attn: AMSEL-RD-MAT 2

Commanding General
U. S. Army Materiel Command
Washington, D. C. 20315
Attn: AMCRD-RC-M 1

Commanding General
U. S. Army Missile Command
Redstone Arsenal, Alabama 35809
Attn: Technical Library 1

Commanding General
U. S. Army Munitions Command
Dover, New Jersey 07801
Attn: Technical Library 1

Commanding General
U. S. Army Tank-Automotive Center
Warren, Michigan 48090
Attn: Tech Data Coord Br., SMOTA-RTS
SMOTA-RCM.1 2

Commanding General
U. S. Army Weapons Command
Rock Island, Illinois 61201
Attn: Research & Development Directorate, AMSWE-RDR 1

DISTRIBUTION LIST

	<u>No. of Copies</u>
Commanding General U. S. Army Satellite Communications Agency, Fort Monmouth, New Jersey 07703 Attn: Technical Document Center	1
Commanding General White Sand Missile Range White Sands, New Mexico 88002 Attn: STEWS-WS-VT	1
Commanding Officer Aberdeen Proving Ground Maryland 21005 Attn: Technical Library, Bldg. 313	1
Commanding Officer U. S. Army Research Office (Durham) Box CM Duke Station Durham, North Carolina 27706	1
Commanding Officer Frankford Arsenal Bridge and Tacony Streets Philadelphia, Pennsylvania 19137 Attn: Library Branch, C-2500 Mr. H. Markus, SMUFA-L7000	1 1
Commanding Officer Picatinny Arsenal Dover, New Jersey 07801 Attn: SMUPA-VA6	1
Commanding Officer Watervliet Arsenal Watervliet, New York 12189 Attn: SWEWV-RDT, Technical Information Services Offices	1
Commanding Officer U. S. Army Aviation Materiel Laboratories Fort Eustis, Virginia 23604	1
Commanding Officer USACDC Ordnance Agency Aberdeen Proving Groun, Maryland 21005 Attn: Library, Bldg. 305	2

DISTRIBUTION LIST

No. of Copies

Commanding Officer U. S. Army Edgewood Arsenal Edgewood Arsenal, Maryland 21010 Attn: Dir. of Eng. & Ind. Serv., Chem-Mun Br., (Mr. F. E. Thompson)	1
Redstone Scientific Information Center U. S. Army Missile Command Redstone Arsenal, Alabama 35809 Attn: Chief, Documents Section	4
U. S. Army Aviation School Library USAAVNS-P&NRI Fort Rucker, Alabama 36360	1
Department of the Army Ohio River Division Laboratories Corps of Engineers 5851 Mariemont Avenue Cincinnati, Ohio 45227 Attn: ORDLB-TR	1
Commanding Officer Army Materials and Mechanics Research Center Watertown, Massachusetts 02172 Attn: AMXMR-AT, Technical Information Branch AMXMR-AA AMXMR-MX, Mr. N. Reed AMXMR-RX, Dr. R. Beeuwkes, Jr. AMXMR-RP, Mr. G. A. Darcy, Jr. AMXMR-TP, Mr. P. A. G. Carbonaro AMXMR-TP, Castings and Cermets Branch	5 1 1 1 1 1 5
American Foundrymen's Society Golf and Wolf Roads Des Plaines, Illinois 60016 Attn: Mr. P. R. Gouwens	1
Case Institute of Technology University Circle Cleveland, Ohio 44106 Attn: Professor J. F. Wallace	1
Dartmouth College Thayer School of Engineering Hanover, New Hampshire 03755 Attn: Professor G. A. Colligan	1

DISTRIBUTION LIST

	<u>No. of Copies</u>
Harvard University Cambridge, Massachusetts 02139 Attn: Professor Bruce Chalmers	1
Investment Casting Institute 3525 West Peterson Road Chicago, Illinois 60645 Attn: Mr. R. E. Pritchard	1
Massachusetts Institute of Technology Cambridge, Massachusetts 02139 Attn: Professor M. C. Flemings	1
Northeastern University 360 Huntington Avenue Boston, Massachusetts 02115 Attn: Professor John Zotos	1
Steel Founders' Society Westview Towers 21010 Center Ridge Road Rocky River, Ohio 44116 Attn: Mr. Charles Briggs	1
Tufts University Medford, Massachusetts 02155 Attn: Professor K. Van Wormer, Jr.	1

<p>AD Accession No. U.S. Army Materials Research Agency, Watertown, Massachusetts 02172 INVESTIGATION OF SOLIDIFICATION OF HIGH-STRENGTH STEEL CASTINGS M. C. Flemings and R. V. Barone Report AMRC CR 63-04/5, Oct 1964 - Sept 1966, 87 pp - tables - illus, AMCS Code No. 5025.11.294, D/A Proj 1C024401A238, Unclassified Report</p> <p>Analytical and experimental work on microsegregation and dendrite structure in a series of iron base alloys is summarized. Experimental work is on iron-nickel alloys, iron-4% phosphorous alloy, iron-25% copper alloy, and iron-nickel carbon alloys.</p> <p>A new computer analysis for microsegregation is presented with detailed numerical results given for iron-25% nickel alloy, iron-10% nickel alloy, and iron-1% phosphorous alloy. Results agree reasonably well with experiment provided the dendrite arm spacing used in calculation is less by a constant "correction factor", g, than that measured (for example $g = 0.40$ for cylinder model, secondary dendrite arm spacing). It is concluded that the need for the correction factor arises primarily because the model employed for calculation does not account for "ripening" during solidification.</p> <p>Structures of the various alloys studied are presented; in some, the dendrite morphology is strongly plate-like; in others, it is "fibrous". Over a range of cooling rates from $10^{-3}^{\circ}\text{C/sec}$ to nearly 10^6°C/sec dendrite arm spacing of iron-25% nickel alloy is linearly related to a single power of cooling rate. It is concluded that the dependency results from the predominant effect of "coarsening" in determining final dendrite arm spacing.</p>	<p>NO DISTRIBUTION LIMITATIONS</p>	<p>AD Accession No. U.S. Army Materials Research Agency, Watertown, Massachusetts 02172 INVESTIGATION OF SOLIDIFICATION OF HIGH-STRENGTH STEEL CASTINGS M. C. Flemings and R. V. Barone Report AMRC CR 63-04/5, Oct 1964 - Sept 1966, 87 pp - tables - illus, AMCS Code No. 5025.11.294, D/A Proj 1C024401A238, Unclassified Report</p> <p>Analytical and experimental work on microsegregation and dendrite structure in a series of iron base alloys is summarized. Experimental work is on iron-nickel alloys, iron-4% phosphorous alloy, iron-25% copper alloy, and iron-nickel carbon alloys.</p> <p>A new computer analysis for microsegregation is presented with detailed numerical results given for iron-25% nickel alloy, iron-10% nickel alloy, and iron-1% phosphorous alloy. Results agree reasonably well with experiment provided the dendrite arm spacing used in calculation is less by a constant "correction factor", g, than that measured (for example $g = 0.40$ for cylinder model, secondary dendrite arm spacing). It is concluded that the need for the correction factor arises primarily because the model employed for calculation does not account for "ripening" during solidification.</p> <p>Structures of the various alloys studied are presented; in some, the dendrite morphology is strongly plate-like; in others, it is "fibrous". Over a range of cooling rates from $10^{-3}^{\circ}\text{C/sec}$ to nearly 10^6°C/sec dendrite arm spacing of iron-25% nickel alloy is linearly related to a single power of cooling rate. It is concluded that the dependency results from the predominant effect of "coarsening" in determining final dendrite arm spacing.</p>
<p>AD Accession No. U.S. Army Materials Research Agency, Watertown, Massachusetts 02172 INVESTIGATION OF SOLIDIFICATION OF HIGH-STRENGTH STEEL CASTINGS M. C. Flemings and R. V. Barone Report AMRC CR 63-04/5, Oct 1964 - Sept 1966, 87 pp - tables - illus, AMCS Code No. 5025.11.294, D/A Proj 1C024401A238, Unclassified Report</p> <p>Analytical and experimental work on microsegregation and dendrite structure in a series of iron base alloys is summarized. Experimental work is on iron-nickel alloys, iron-4% phosphorous alloy, iron-25% copper alloy, and iron-nickel carbon alloys.</p> <p>A new computer analysis for microsegregation is presented with detailed numerical results given for iron-25% nickel alloy, iron-10% nickel alloy, and iron-1% phosphorous alloy. Results agree reasonably well with experiment provided the dendrite arm spacing used in calculation is less by a constant "correction factor", g, than that measured (for example $g = 0.40$ for cylinder model, secondary dendrite arm spacing). It is concluded that the need for the correction factor arises primarily because the model employed for calculation does not account for "ripening" during solidification.</p> <p>Structures of the various alloys studied are presented; in some, the dendrite morphology is strongly plate-like; in others, it is "fibrous". Over a range of cooling rates from $10^{-3}^{\circ}\text{C/sec}$ to nearly 10^6°C/sec dendrite arm spacing of iron-25% nickel alloy is linearly related to a single power of cooling rate. It is concluded that the dependency results from the predominant effect of "coarsening" in determining final dendrite arm spacing.</p>	<p>NO DISTRIBUTION LIMITATIONS</p>	<p>AD Accession No. U.S. Army Materials Research Agency, Watertown, Massachusetts 02172 INVESTIGATION OF SOLIDIFICATION OF HIGH-STRENGTH STEEL CASTINGS M. C. Flemings and R. V. Barone Report AMRC CR 63-04/5, Oct 1964 - Sept 1966, 87 pp - tables - illus, AMCS Code No. 5025.11.294, D/A Proj 1C024401A238, Unclassified Report</p> <p>Analytical and experimental work on microsegregation and dendrite structure in a series of iron base alloys is summarized. Experimental work is on iron-nickel alloys, iron-4% phosphorous alloy, iron-25% copper alloy, and iron-nickel carbon alloys.</p> <p>A new computer analysis for microsegregation is presented with detailed numerical results given for iron-25% nickel alloy, iron-10% nickel alloy, and iron-1% phosphorous alloy. Results agree reasonably well with experiment provided the dendrite arm spacing used in calculation is less by a constant "correction factor", g, than that measured (for example $g = 0.40$ for cylinder model, secondary dendrite arm spacing). It is concluded that the need for the correction factor arises primarily because the model employed for calculation does not account for "ripening" during solidification.</p> <p>Structures of the various alloys studied are presented; in some, the dendrite morphology is strongly plate-like; in others, it is "fibrous". Over a range of cooling rates from $10^{-3}^{\circ}\text{C/sec}$ to nearly 10^6°C/sec dendrite arm spacing of iron-25% nickel alloy is linearly related to a single power of cooling rate. It is concluded that the dependency results from the predominant effect of "coarsening" in determining final dendrite arm spacing.</p>